Chapter 14

Lidar Backscatter Depolarization Technique for Cloud and Aerosol Research

Kenneth Sassen
Department of Meteorology
University of Utah
Salt Lake City, Utah 84112

I. INTRODUCTION

The interaction of light with aerosols, or cloud and precipitation particles (i.e., hydrometeors), as often vividly revealed in a variety of optical displays, has long intrigued scientific observers and led to fundamental advances in the field of optical physics. The appearance of halo arcs, rainbows, and coronas, to name but a few impressive celestial occurrences, actually represents concentrations of reflected, refracted, or diffracted natural light in the scattering phase functions of

Light Scattering by Nonspherical Particles: Theory, Measurements, and Applications

hump in their individual Köhler curve. Thus, young hydrometeors scatter light in the Rayleigh–Mie transition zone until continued growth elevates them to the quiescent geometrical optics realm, where scattering is related to the cross-sectional area. As we shall see, this transition has recently been the subject of considerable theoretical work, along with pioneering lidar research.

Basic Stokes $\{I, Q, U, V\}$ parameterization has been discussed in Chapter 1. For our purposes, we begin with the representation of radiation scattered into the exact backscattering direction from polarized laser light, where, after simplifying assumptions, the scattering matrix is given by (Mishchenko and Hovenier, 1995)

$$\mathbf{F}(180°) = \mathrm{diag}[F_{11}(180°), F_{22}(180°), F_{33}(180°), F_{44}(180°)]. \quad (1)$$

The assumptions are that the nonspherical particles are randomly arrayed in three-dimensional (3D) space and that they display a reasonable symmetry and/or shape diversity. (Obviously, this is violated when ice crystals assume preferred orientations, as they often do, but the alternative leads potentially to the consideration of all 16 matrix elements.) Next we define a scattering plane with reference to the laser beam, which is 100% linearly polarized parallel to this plane. Then, the Stokes vector is proportional to $\{1, 1, 0, 0\}$ and the linear depolarization ratio δ (also expressed as LDR), or the ratio of the perpendicular-to-parallel polarization components of backscattered light, is given by

$$\delta = \frac{F_{11}(180°) - F_{22}(180°)}{F_{11}(180°) + F_{22}(180°)}. \quad (2)$$

Because for spheres $F_{11}(180°) = F_{22}(180°)$, we get the well-known finding of $\delta = 0$ for single scattering by cloud droplets.

Finally, although not yet well exploited (Woodard *et al.*, 1998), lasers transmitting circularly polarized light can measure the circular depolarization ratio δ_c (or CDR), given in terms of δ as (Mishchenko and Hovenier, 1995)

$$\delta_c = \frac{2\delta}{1 - \delta}. \quad (3)$$

A range of other depolarization combinations, such as linear analyses from circular polarization (as also pioneered in microwave radar studies), are possible and can be similarly defined. It should also be mentioned that direct measurements of Stokes parameters have been attempted in both the field (Houston and Carswell, 1978) and the laboratory (Griffin, 1983).

We show in Fig. 1 a schematic view of the distinct backscattering mechanisms for a sphere and a hexagonal ice crystal model according to ray optics theory. Here the physical optics explanation of the Stokes theory becomes apparent. In the geometric optics domain, spheres backscatter through a combination of surface waves (trapped at the dielectric interface) and axial reflections off the front and far drop faces, none of which produce depolarization. An ice crystal prism, on

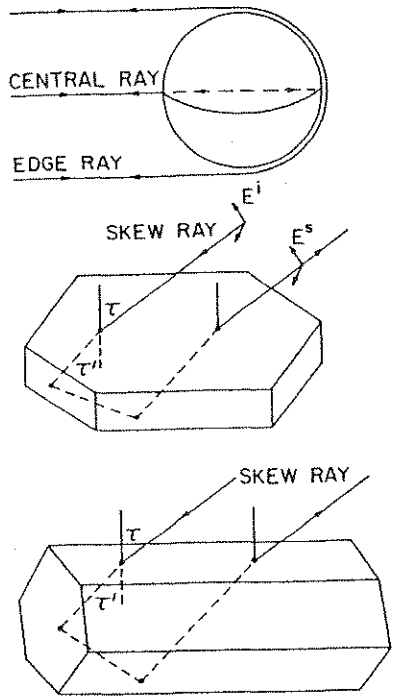

Figure 1 Geometric optics view of the light ray paths responsible for backscattering from a spherical water drop, contrasted to the internal skew rays for simple plate and column ice crystal models. Reprinted from K.-N. Liou and H. Lahore (1974), Laser sensing of cloud composition: A backscattered depolarization technique, *J. Appl. Meteorol.* **13**, 257–263. Copyright © 1974 American Meteorological Society.

the other hand, may produce a nondepolarizing specular reflection when a crystal face is fortuitously aligned perpendicular to the laser beam direction, but it is considerably more likely that (except for scattering geometries involving particles with fixed orientations) internally refracted and reflected ray paths will be chiefly responsible for backscattering. These processes result in the reorientation of the incident polarization vector at every interface, leading to depolarization when the backscattered ray is transposed into the initial plane of polarization.

Finally, as an overview of the range of hydrometeor depolarizing behaviors, we present in Fig. 2 data collected by a helium–neon (HeNe) continuous-wave (CW) laser–lidar analog device in the laboratory and field during the early 1970s to help evaluate the potential of lidar for cloud physics research (see the review by Sassen, 1991). Although we will often revisit the issue of hydrometeor identification in

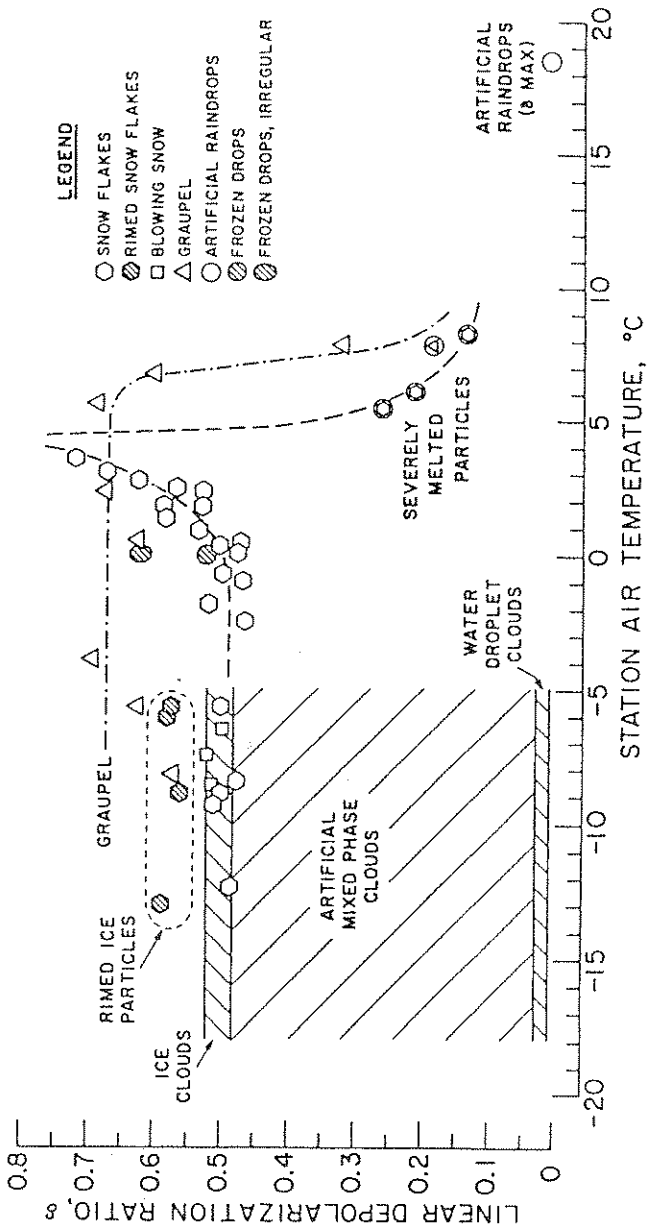

Figure 2 Results of early laboratory and field studies using a CW laser–lidar analog device, showing the great range of linear depolarization ratios encountered from various types of hydrometeors. Reprinted from K. Sassen (1991), The polarization lidar technique for cloud research: A review and current assessment, *Bull. Am. Meteorol. Soc.* **72**, 1848–1866. Copyright © 1991 American Meteorological Society.

later sections, at this point it is useful to consider backscattering from nonspherical and irregular particles from the geometric optics viewpoint. The hatched regions in Fig. 2 are from early laboratory experiments and confirm the basic utility of the LBDT, that is, cloud phase discrimination. Whereas laboratory supercooled water clouds produce near-zero δ, the simple ice clouds artificially nucleated from them generate $\delta \approx 0.5$; not surprisingly clouds of mixed water–ice composition generated intermediate values.

Importantly, when precipitating ice particles were probed from out of a laboratory window, the LBDT was shown to enable the separation of various ice particle types. Snowflakes, composed essentially of randomly oriented dendritic ice crystals, tend to produce the same $\delta \approx 0.5$ as randomly oriented laboratory crystals of generally mixed habits. However, as frozen cloud droplets begin accumulating on the ice crystal faces, the increase in surface complexity leads to a depolarization increase. Ultimately, the droplet accretion process results in the formation of low-density graupel particles, or even hailstones under the proper conditions. Graupel data are shown by the triangle symbols in Fig. 2, where it can be seen that these opaque aspherical particles generate $\delta \approx 0.65$. The action of the final microphysical process, hydrometeor melting, is revealed to produce a strong increase in depolarization for snowflakes, but graupel are unaffected. This again appears to be due to changes in surface complexity; whereas graupel internally absorb melt water and do not appear to change shape much, snowflake surfaces become rounded, compacted, and coated unevenly by water. The additional changes that occur during the final stages of melting show the expected transition from inhomogeneous to pure water drops, but hidden scattering effects explainable by geometric optics theory will be revealed later.

It is not inappropriate to suggest here that the LBDT is akin to human perception in its ability to clearly identify differences in particle shape—certainly the wavelengths used for probing are the same.

III. POLARIZATION LIDAR DESIGN CONSIDERATIONS

Although a detailed discussion of polarization lidar technology is clearly beyond the scope of this chapter, lidar design considerations have consequences for both data collection and interpretation. Unlike some lidar techniques that rely on advanced spectroscopic hardware, polarization diversity requires only the assembly of off-the-shelf components, namely, commercial laser sources (chiefly Nd:YAG and ruby), telescopes, and detector packages that are tailored to the laser wavelength. Only the simple addition of a polarization beam-splitting prism just behind the focal plane aperture along with an extra detector is needed for two-channel polarization measurements. In Fig. 3 is an example of the design

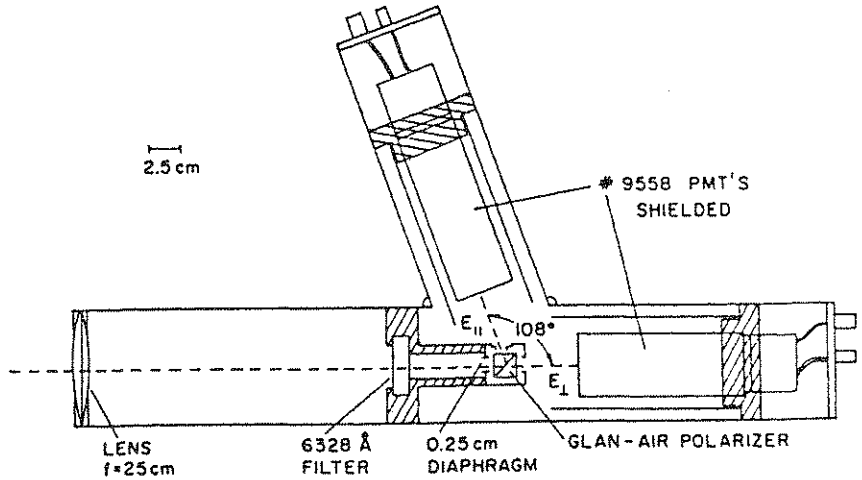

Figure 3 Typical polarization lidar receiver design using a polarizing prism and dual photomultiplier tube (PMT) detectors to permit simultaneous depolarization measurements. This example is for a laboratory lidar analog receiver, and so has a forward collecting lens. Reprinted from K. Sassen (1974), Depolarization of laser light backscattered by artificial clouds, *J. Appl. Meteorol.* **13**, 923–233. Copyright © 1974 American Meteorological Society.

of a dual-polarization receiver, in this case from a CW laser–lidar analog device (Sassen, 1974), which substitutes a light-collecting lens for the reflector used in pulsed lidar systems. The standard receiver components are a laser line interference filter (to block out background solar scattering), a field-of-view (FOV) limiting aperture and polarizer prism (in this case a Glan-air calcite cube) placed at the receiver focal point, and the dual detectors. In this example, two extended S-20 photomultiplier tubes were used to detect the backscattered 0.633-μm HeNe laser light. Although this design dates from the early 1970s, it remains in vogue today.

For polarization applications, the use of steering mirrors for directing the laser beam is unwise in order to avoid unnecessarily corrupting the transmitted and received polarization properties. Thus, polarization lidars usually involve placing the laser and telescope side by side on a stable table that is pointed into the vertical direction, after assuring the parallel alignment of the two beams. (Alternatively, a 45° mirror can be used to direct the beam into the receiver FOV.) Shown in Fig. 4 is a photograph of our turnkey ruby (0.694-μm) lidar system at the University of Utah Facility for Atmospheric Remote Sensing (FARS), which uses the receiver design of Fig. 3 and the side-by-side configuration on a (manually) steerable table supported by a yoke. The ability to steer the lidar is important to aid in beam alignment (with the use of a distant target board and steerable collimator), but also for allowing the collection of off-zenith measurements from ice clouds to

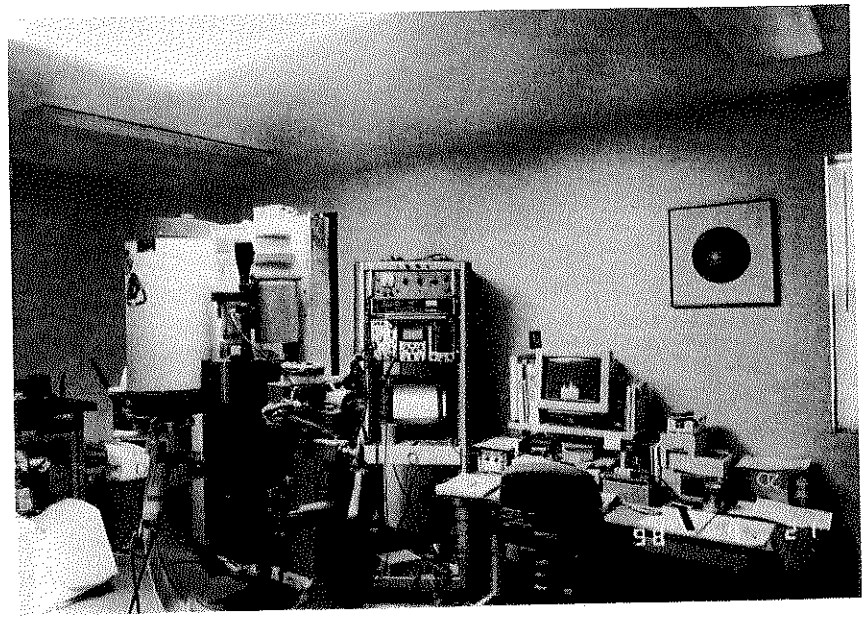

Figure 4 Photograph of a basic polarization lidar installation, at the University of Utah Facility for Atmospheric Remote Sensing. The PC-controller station is visible at right; at left are the laser transmitter, telescope receiver, and infrared radiometer units mounted on a table supported by a yoke to permit scanning.

identify anisotropic scattering conditions, as explained later. Note from Fig. 4 the placement of the collimator directly in front of the laser, and adjacent to it, the coaligned PRT-5 infrared radiometer. Data acquisition and storage for this system is accomplished simply, using a digital storage oscilloscope and a personal computer (PC) with 8-mm tape backup. This facility was built specifically for remote-sensing studies and has an opening skylight for the lidar and a roof parapet for mounting a variety of supporting radiometers and cameras.

The divergence of the laser beam and the FOV of the receiver defined by the aperture have important consequences for polarization data interpretation. Owing to the finiteness of these angles, the effects of laser pulse attenuation differ from that predicted by the Beer–Lambert law for an infinitely narrow divergence angle. This not only complicates quantitative data analysis for standard lidar systems, but also impacts on depolarization analysis through the viewing of multiply scattered radiation by the receiver. On the other hand, this aspect could be used to help interpret lidar signals when the FOV is rapidly changed. Other improvements could be the addition of multiwavelength depolarization measurements for

studying particles in the Rayleigh–Mie transition region and for differential reflectivity observations. In general, the widely used Nd:YAG laser transmitters are well suited for aerosol and cloud research. With frequency doubling, simultaneous 10-Hz outputs at 1.06 and 0.532 μm are on the order of 1 J, with an approximately 10-ns pulse length and 1.0-mrad divergence angle. Fast (up to 100 MHz) data digitization boards to take advantage of such high spatial and temporal resolutions are commercially available, although they are currently limited to 8-bit resolution. Details of the design of a modern lidar system combining these attributes, the University of Utah Polarization Diversity Lidar (PDL), are given in Sassen (1994).

Still more advanced lidar systems incorporating spectroscopic technologies have added polarization diversity, such as the turnkey Raman water vapor lidar system routinely operated at the Southern Great Plains Cloud and Radiation Testbed (SGP CART) site in north-central Oklahoma (Goldsmith *et al.*, 1998). Because it is relatively straightforward to add depolarization receiver channels, the amount of extra information gained is economical. Methods that can increase cloud/aerosol information, and improve spectroscopic data quality in some cases, include Raman scattering, high spectral resolution lidar (HSRL), differential absorption lidar (DIAL), and even the new near-infrared Doppler lidars (for reviews, see Carswell, 1983; Ansmann *et al.*, 1993; Sassen, 1995). Moreover, considerable expertise is required to fabricate eye-safe, low-power, unattended laser ceilometers to routinely monitor cloud heights, and dual-polarization capabilities also have considerable advantages in this regard as well (Spinhirne, 1993).

The basic lidar equation for polarization applications was provided early on in Schotland *et al.* (1971) for the case of isotropic scattering media:

$$P_{\perp,\parallel}(R) = P_0\left(\frac{ctA_r}{2R^2}\right)\beta_{\perp,\parallel}(R)\exp\left[-2\eta\int\sigma(R)\,dR\right], \tag{4}$$

where the subscripts $\perp$ and $\parallel$ refer to the planes of polarization perpendicular and parallel to the incident (vertical by convention) polarization plane, R is the range, P_0 the linearly polarized output power, c the speed of light, t the laser pulse length, A_r the receiver collecting area, β the backscattering coefficients per unit volume (in units of per length per steradian), η the multiple-scattering correction factor that accounts for "captive diffraction" (usually taken out of the integral for simplicity), and σ is the extinction coefficient per unit volume (per length). The integral is taken over the range of R_0 ($R = 0$) to R.

The linear depolarization ratio δ can now be expressed from the ratio of the polarized lidar equations as

$$\delta(R) = \frac{P_\perp(R)}{P_\parallel(R)} = \frac{\beta_\perp(R)}{\beta_\parallel(R)}, \tag{5}$$

which is reduced simply to the ratio of the backscattering coefficients.

Although not recently given much attention, Eqs. (4) and (5) can be violated under conditions associated with the anisotropic scattering medium of uniformly oriented ice crystal populations, and δ values even exceeding unity have been reported in the field (Derr *et al.*, 1976; Sassen, 1976). Could the assumption that σ is independent of the polarization state be incorrect owing to the birefringence property of ice and pulse propagation effects? Although Takano and Jayaweera (1985) have indicated that $\delta \gtrsim 1.0$ is theoretically possible for some combinations of lidar observation angle and crystal axis ratio and orientation, the great δ increases noted to occur with penetration depth into some ice clouds suggest that more than single backscattering is involved. Perhaps, the transmission of light directly through horizontally oriented ice plates (see Sassen, 1987a) at most lidar angles, coupled with birefringence-induced depolarization, creates an increasingly altered pulse polarization state owing to this form of forward scattering. At microwave radar frequencies, propagation effects through regions of oriented particles can have major impacts, and represent a mainstay of attempts to infer target composition. To account for such effects, Schotland *et al.* (1971) gave the following broader definition for the linear depolarization ratio in terms of the atmospheric transmission terms τ in the two polarization planes:

$$\delta(R) = \frac{\beta_\perp(R)}{\beta_\parallel(R)}\exp(\tau_\parallel - \tau_\perp). \tag{6}$$

Because lidar depolarization may be influenced by the polarization corruption of the forward and backscattered laser pulses during transmission, this is a research area that will no doubt receive more attention using scanning lidars.

Finally, it is important to note that the lidar backscattering and extinction coefficients actually represent the range-dependent sums of the contributions from all the atmospheric constituents present, including molecular, aerosol, and hydrometeor scatterers, although when present cloud scattering would typically dominate. Moreover, and importantly, the preceding equations apply only to the single-scattering case, and so additional backscattering terms (Sassen and Zhao, 1995) must be considered in the probing of most clouds in our atmosphere.

IV. AEROSOL RESEARCH

Surprisingly, relatively little lidar research has been directed toward the study of nonspherical or inhomogeneous aerosols in the troposphere using the depolarization method. This is partly the result of the great difficulties inherent in separating the weakly depolarizing ($\delta \sim 0.02$) molecular returns (Hohn, 1969) from the aerosol signal using simple two-channel lidars (see the following for a discussion of the promise of more advanced techniques), but may also reflect a lack of recognition of the potential benefits. Polarization studies of the background

and polluted lower troposphere, particularly in conjunction with HSRL or Raman measurements to separate out the molecular constituents, hold particular promise for characterizing the content of such climatically important aerosols.

Boundary layer aerosol research is further complicated by the effects of relative humidity, which causes hygroscopic aerosols to deliquesce and swell into spherical haze particles. Such wetted particles may have solid inclusions and odd refractive indices, but will generate near-zero δ because of the relatively minute particle sizes. Thus, the δ values from hygroscopic particles will decrease as the relative humidity increases (Murayama *et al.*, 1997). As for the dry particulates, their depolarizing properties will depend on their size, composition (i.e., refractive index and uniformity), and shape (McNeil and Carswell, 1975; Kobayashi *et al.*, 1985, 1987). Because boundary layer aerosols may comprise a mixture of non- and hygroscopic particles of various materials over a large size range, particularly in urban areas, this scattering "soup" presents significant problems in quantitative lidar signal analysis, but polarization diversity in combination with spectroscopic techniques could be of great benefit.

Occasionally, dense (i.e., relative to molecular scattering) aerosol layers in the free troposphere are created by catastrophic local or regional events, such as fierce dust storms or fires. Plate 14.1 (see color Plates 14.1–14.5) shows an image of an Asian (Kosa) dust storm, as the particulates were swept up into a developing weather system and advected over a polarization lidar in Tokyo, Japan (Murayama *et al.*, 1998). Present in the returned energy display are sporadic strongly scattering cirrus clouds between 9 and 12 km, streaks of Kosa dust descending from approximately 11 km, and the aerosol of the boundary layer in the lowest kilometer. In terms of depolarization, the cirrus produced $\delta \approx 0.45$, the dust between 0.1 and 0.2, and the low-level aerosol less than 0.1. Note that the strongest returns in the boundary layer correspond to $\delta > 0.05$, which are regions of activated haze particles. In contrast, the significant depolarization in the Kosa dust, despite their relatively weak backscattering, indicates that they are crystalline particles. One may ask whether these potential cloud nuclei may have interacted with the cirrus clouds clearly embedded in the dust plume.

The example of a smoke plume created by a brush/forest fire approximately 25 km upwind of the FARS site in Plate 14.2 depicts a more dynamic microstructure in the dense aerosol cloud, which had a milky, bluish appearance. The layer is quite irregular, indicative of variations in the fire conditions that created the plume, and also perhaps preserving gravity waves. Toward the end of the display, a tongue of aerosols descends toward the surface (at 1.52 km above mean sea level, MSL) during a period of plume fumigation. The corresponding δ values decrease with height in the smoke layer: $\delta < 0.025$ are found at the layer top, whereas values up to 0.10 occur at the bottom, particularly near the end of the period. We conclude that the backscattering was dominated by spherical haze particles from condensed water and organic vapors in the upper regions of the layer, but that

relatively large and irregular ash particles were in the process of sedimenting out of the layer, perhaps aided by coagulation. Following these observations, a light coating of gray ash was noted on the lidar telescope window.

It is particularly with regard to researching the aerosols of the stratosphere that polarization lidar has played a leading role (Iwasaka and Hayashida, 1981). Because the distinction between stratospheric clouds and aerosols is sometimes vague, as the particles remain small in response to limited growth opportunities and rapid fallout in the thin air, we will consider both here. Principally, stratospheric scatterers can be divided into (i) the background aerosol dominated by (spherical) aqueous sulfuric acid droplets generated photochemically *in situ*; (ii) the apparently uncommon polar stratospheric clouds (PSCs) of various types often connected to ozone depletion; and (iii) the occasional volcanically injected aerosols composed of sulfuric acid droplets, ash, and possibly frozen particles. The major aerosol/cloud forming materials include compounds derived from sulfuric and nitric acids admixed with water, providing a rich tableau for theoretical chemists.

Spherical, homogeneous acid droplets must generate $\delta \approx 0$, and so are easily identified (Sassen and Horel, 1990). Frozen multisubstance particles, however, will depolarize visible laser light not only to the degree dictated by their amount of nonsphericity but also according to their size: Stratospheric particles tend to reside in the Rayleigh–Mie transition region with regard to light scattering. A number of theoretical studies have shown that variations in δ measured at a given wavelength are highly sensitive to the particle size parameter, which represents a significant complication to single-wavelength lidar analyses (Mishchenko and Sassen, 1998). Based largely on lidar studies, three distinct types of PSCs have been identified, although the question of the precise corresponding particle compositions has not been settled by theoretical chemists (Poole *et al.*, 1990). Recently, it has also been demonstrated that ice crystal clouds generating strong depolarization can also inhabit the Antarctic middle stratosphere (Gobbi *et al.*, 1998).

The fate of volcanically produced aerosols in the lower stratosphere (LS) and upper troposphere (UT) also involve chemical processes. Based on laboratory studies (Sassen *et al.*, 1989a), the neutralization and partial crystallization of sulfuric acid drops from the absorption of ammonia gas of lower-tropospheric origin was shown to generate $\delta \sim 0.1$ for micrometer-sized particles, which were similar to lidar measurements in an unusual volcanic aerosol layer injected into the UT over Central America and later studied over Salt Lake City, Utah (Sassen and Horel, 1990). Also unexpected were the δ values of approximately 0.05 measured in the LS following the 1991 Mt. Pinatubo volcanic eruptions at times of unusually cold midlatitude tropopause temperatures in conjunction with Bishop's ring observations (Sassen *et al.*, 1994a). It was conjectured that nonspherical submicrometer-sized frozen sulfuric acid tetrahydrate (SAT) particles could have been responsible for the optical display and nonzero δ values.

Finally, the case of aircraft condensation trail (contrail) formation in the UT bridges the Rayleigh–Mie transition and geometric optics regimes, and so provides a strict test of polarization lidar analysis methods, as well as a great deal of promise for remote sensing of particle characteristics. A theoretical study specifically addressing this problem using a uniquely wide selection of nonspherical particle shapes and aspect ratios (Mishchenko and Sassen, 1998) has revealed that polarization lidar, particularly dual-wavelength systems, has significant potential for sizing the rapidly growing contrail particles. For nearly all particles modeled, a backscatter depolarization resonance region was found for effective size parameters of approximately 10–15 (corresponding to an ~1-μm particle radius at the 0.532-μm laser wavelength), which produced the highest δ values. Because $\delta < 0.01$ were predicted for effective size parameters of less than approximately 5, the rapid δ changes as the contrail particles grow through the scattering regime transition zone should allow for valuable research using sufficiently high resolution polarization lidars (Sassen and Hsueh, 1998).

V. WATER AND MIXED-PHASE CLOUD RESEARCH

The simplest application of the LBDT is the identification of clouds composed of spherical cloud droplets. This follows from the null detection of the cloud base region in the depolarized channel, before the buildup of multiply scattered depolarization gradually is manifested with penetration depth. The cause of the depolarization is related mainly to the polarization properties of azimuthally scattered light from spheres at near-backscattering angles, in combination with double scattering that redirects the light into the receiver FOV (Carswell and Pal, 1980). This process is controlled essentially by the size of the instantaneous scattering volume (i.e., FOV and range to cloud) and the cloud droplet number size distribution. Although most theoretical simulations based on the lidar geometry show a rather monotonic δ increase, this appears to be a consequence of the unrealistic treatment of water cloud content as vertically homogeneous targets. Consideration of the evolution of cloud droplet sizes with height yields important insights into multiple scattering in water clouds (Sassen and Zhao, 1995). By significantly restricting the lidar FOV on the order of 160 μrad these depolarizing effects can be largely negated (Eloranta and Piironen, 1994).

We provide in Plate 14.3 an example of the results of varying the receiver FOV while the laser illuminates a pure water phase layer studied by our PDL system at the Oklahoma CART site. Depicted is a height–time display of parallel-polarized relative 0.532-μm backscattering of the thin (~140 m) stratus cloud, along with the corresponding linear depolarization ratio display (note inserted color δ key). Over the indicated 5-min period the receiver FOV was gradually decreased in

10 steps from 3.8 to 0.28 mrad (the transmitter divergence was 0.45 mrad). Despite some variability that reflects the microphysical changes associated with the cellularity in cloud structure, it is clear that the peak depolarization steadily decreases with decreasing FOV from approximately 0.35 to 0.05. Also note that δ decreases rapidly near the cloud top in response to evaporation, as droplet sizes decrease during the mixing process with the dry air above.

To the polarization lidar experimentalist, spheres may be boring, but the situation becomes more interesting when both water and ice exist in a supercooled cloud layer. As illustrated in mixed-phase cloud model studies (Sassen *et al.*, 1992), supercooled water clouds cannot contain a relatively large amount of ice for long, for the competing and more rapid ice phase growth occurs at the expense of the cloud droplets and the water vapor needed for their growth. As a result, as the ice content in a supercooled mixed-phase cloud increases, the LDR within the cloud actually decreases because of a lessening of the effects of multiple scattering using the usual (1–3-mrad) lidar receiver FOVs in the model. Thus, simple polarization techniques do not show much promise in quantitatively separating the ice and water contents in mixed-phase clouds.

Although clouds that produce precipitation reaching the ground are discussed later, polarization lidar has unique capabilities for studying thin supercooled cloud layers that produce *virga*, or precipitating particles that do not reach the ground. Under such conditions, lidar detects the weak signals from sedimenting ice particles below the much stronger returns upon entering the water cloud. In terms of δ values, the ice virga may produce the typical 0.4–0.5 values for randomly oriented ice crystals, but often displays the near-zero ratios (when probed in the zenith direction) indicative of horizontally oriented planar crystals (see the following discussion). Of course, water clouds display the characteristic multiple-scattering δ-value increasing trend with penetration depth as a function of the lidar FOV, the signature of this process. Thus, scanning polarization lidar can unambiguously identify these common midlevel cloud conditions, which pose a special problem in attempts to use radar units to characterize clouds. Because even research-grade millimeter wave radars would have great difficulty in detecting the supercooled cloud droplets, the radar would only detect the diffuse ice virga composed of relatively large ice particles, and hence misidentify the cloud system by ignoring the radiatively more important water cloud.

Perhaps the most trying meteorological conditions to interpret involve determining the structure and composition of winter mountain storm cloud systems, which have received much attention because of their potential for artificial cloud seeding to increase snowfall amounts (Sassen *et al.*, 1990a). Snowfall and/or fog are common at mountain side field sites during the cloud seeding experiment periods, and so simple cloud retrieval algorithms relying on subcloud clear air conditions are useless. Lidar returns from supercooled liquid water (SLW) cloud layers embedded in such diverse media are made difficult to identify because of

the potentially strong attenuation in the snowfall below, and of course may often go undetected with lidar if the attenuation is strong enough. Nonetheless, the versatility of the LBDT has been amply illustrated by lidar studies of orographic storm clouds. In addition to identifying liquid-dominated SLW and mixed-phase clouds, applying the principles of hydrometeor shape, surface complexity governing backscatter depolarization, and orientation allows the discrimination of graupel, rimed and pristine snowflakes, and uniformly oriented ice crystals. Such capabilities are important for cloud seeding research because the locations (and temperatures) of SLW clouds and the growth mechanism of precipitation particles are closely tied to the likelihood of the successful introduction of artificial ice nuclei.

VI. CIRRUS CLOUD RESEARCH

As demonstrated early on (Schotland *et al.*, 1971), the differences in δ between water and ice clouds were so dramatic that there was little doubt that cloud thermodynamic phase discrimination was inherent in the LBDT, which is quite important because such clouds at high altitudes have distinct radiative effects (Sassen *et al.*, 1985). This recognition came at a critical time, as it was becoming apparent that the extensive cirrus cloud layers, which covered a significant portion of the globe, would likely have a major impact on our climate and on how our atmosphere would respond to the hypothesized changes brought about by the buildup of greenhouse gases through cloud feedback mechanisms (Liou, 1986). The next step was to evaluate the information content of depolarization variations in ice clouds, and this effort gained impetus in the 1980s as scientific attention became focused on cirrus clouds in order to better understand their impact on the planet's radiation balance (Sassen *et al.*, 1990b). Ray-tracing theory has clearly demonstrated that δ values depend critically on the hexagonal ice crystal axis ratio (Takano, 1987; Takano and Liou, 1995) and that preferentially oriented crystals generate lidar elevation angle-dependent δ values (Takano and Jayaweera, 1985). For example, it can be seen from Table I that δ can vary from about 0.3 for randomly oriented thin plates to 0.6 for solid columns. In other words, δ increases with increasing axis ratio, and when the effects of the birefringence property of ice are also considered, the δ_b values in Table I tend to be somewhat stronger. Thus, according to theory, polarization lidar should have the capability of discriminating between basic ice crystal types. Experimental differences depending on crystal habit were also apparent in the field and laboratory (see the review in Sassen, 1991).

However, the situation in nature seems to have limited these laser remote-sensing opportunities, because most cirrus (off-zenith) measurements reveal δ in the 0.4–0.5 range. It appears that, as indicated by direct *in situ* particle sampling

Table I

Backscatter Linear Depolarization Ratio Values at Visible Wavelengths Computed Through Ray Tracing for Randomly Oriented Solid Ice Crystals with the Indicated Length L to Radius a Ratios (in μm). The Two Columns Show the Results Computed Ignoring (δ) and Including (δ_b) Ice Birefringence Effects

$L/2a$	δ	δ_b
8/80 (thin plate)	0.339	0.399
16/80 (plate)	0.355	0.396
32/80 (thick plate)	0.394	0.508
64/80 (short column)	0.382	0.500
200/80 (column)	0.550	0.616
400/80 (long column)	0.563	0.611

Source: Adapted from Takano (1987).

(Sassen *et al.*, 1994b), cirrus ice crystal collections often show a great diversity in particle habits and axis ratios reflecting dynamic cloud processes involving a combination of vertical redistribution (from vertical air motions and sedimentation), turbulent mixing, and new particle generation, as shown by two-dimensional (2D) model simulations (e.g., Khvorostyanov and Sassen, 1998). Thus, opportunities to probe homogeneous ice cloud compositions may be uncommon, although speculations as to the content of particular regions of cirrus clouds have been widespread. For example, in Sassen *et al.* (1989b), regions associated with Doppler radar-detected updrafts yielded rather low δ (~0.2–0.3), which were attributed either to rapidly growing haze particles, as precursors to new ice particles, or to the peculiar shapes of newly formed ice crystals. Atypically high δ (~0.5–0.8) were measured at the tops of unusually cold, corona-producing midlatitude cirrus layers extending slightly into the LS and also in contact with tropopause folds (Sassen *et al.*, 1995). These high δ values were attributed to the effects on ice particle nucleation and growth of homogeneously frozen sulfuric acid droplets of stratospheric/volcanic origin. Recently, *in situ* sampling of a cold corona-producing cirrus layer (Sassen *et al.*, 1998) revealed the presence of small (~20 μm diameter) simple ice crystals, but the question of the high-δ particle shape has not yet been fully resolved.

Microphysically, a ubiquitous ice cloud polarization lidar application deals with the anisotropic scattering behavior of horizontally oriented planar ice crystals, which initially led to the misidentification of an ice altostratus layer as mixed phase using zenith lidar (Platt, 1977), but soon offered promise in understanding the fall attitudes of atmospheric ice plates (Platt, 1978; Platt *et al.*, 1978). Because

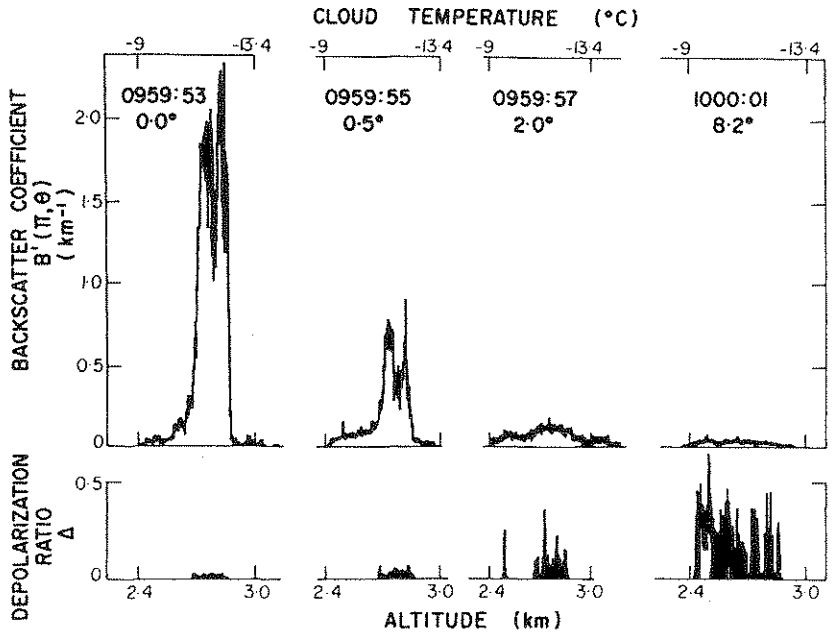

Figure 5 Changes in lidar backscattering and depolarization in a medium of horizontally oriented ice plate crystals produced as the lidar is scanned away from the zenith direction by the indicated amounts. Reprinted from K. Sassen (1991), The polarization lidar technique for cloud research: A review and current assessment, *Bull. Am. Meteorol. Soc.* **72**, 1848–1866. Copyright © 1991 American Meteorological Society.

of this orientation effect and other temperature- and humidity-dependent factors controlling ice crystal shape that could yield increased depolarization (as in Table I), δ-value climatologies of cirrus clouds typically show a trend of increasing δ values with decreasing temperature/increasing height (Platt *et al.*, 1987, 1998). Provided in Fig. 5 is an example of the lidar pointing angle-dependent backscattering and depolarization properties caused by oriented plate crystals. Because of the typically small crystal wobble angles from the horizontal plane (typically $\sim$2.5°), it is only necessary to tip the lidar a few degrees off the zenith to observe often greatly decreased backscatter and increased depolarization. This behavior is undoubtedly due to the coexistence of randomly oriented crystals of different size or habit (Takano and Jayaweera, 1985). Because the specular reflection is approximately 360 times stronger than the backscattering from a sphere of equivalent cross section according to Sassen (1977a), there need not be many of the oriented plates to generate noticeable effects. For example, assuming a $\delta = 0.5$ value for an ice cloud, a simple model predicts that the ratio of unoriented-to-oriented crystals need be only 1/2000 to produce $\delta \approx 0.45$, 1/200 for $\delta \approx 0.25$, and 1/75 for $\delta \approx 0.15$.

Finally, in Plate 14.4 is a unique view of the disorientation of aerodynamically oriented plate crystals apparently caused by turbulent air motions associated with breaking Kelvin–Helmholtz waves in a thin layer embedded within a cirrus cloud system derived from the blowoff of hurricane Nora in September 1997, which basked in the unusually warm El Niño waters off the southern California coast before sending inland a huge cirrus cloud shield that rapidly crossed the continent. This cirrus cloud layer generated vivid and relatively uncommon optical displays, including the 22° halo, perihelia of 22° and 120°, a parhelic circle, and an upper tangent arc/Parry arc combination (see inserted photograph). And what of the ice crystal shapes that were responsible for the near-zero δ values and optical displays? A group of ice crystals collected *in situ* under these conditions is included in Plate 14.4: The hexagonal and rare triagonal particles are solid, have sharp edges, and are often large enough ($\gtrsim$100 μm) to maintain their preferred horizontal orientations, all necessary halo arc-generating virtues. In addition, some plates show an asymmetrical division of prism faces, and if this also occurs for the large columns (imperfectly preserved in the replicator fluid), then it may be possible to explain how the crystals could maintain the so-called Parry arc orientation (Können and Tinbergen, 1998).

VII. PRECIPITATION AND THE PHASE CHANGE

It is no coincidence that this appraisal of polarization lidar applications for cloud research ends with the consideration of the physics of precipitation, for in the study of various precipitation mechanisms we are confronted with the most stringent tests for understanding the backscatter depolarization behaviors of the full range of hydrometeors. Take the case of raindrops at the surface that began their descent as snowflakes aloft. In passing through the freezing level the low-density ice particles gradually melt to produce irregular, mixed-phase particles, followed by the collapse of wet snowflakes into inhomogeneous, ice-containing raindrops, which may be spherical to aspherical depending on the diameter. This is the environment of the microwave radar "bright band." Rainfall and drizzle can also be produced entirely through the liquid phase droplet coalescence process, which should produce depolarization only through multiple scattering. Drizzle precipitation should produce especially low amounts of depolarization, because the concentrations of the drops are typically low and the particles are small enough ($\lesssim$100 μm) to scatter as perfect spheres (unlike aerodynamically distorted raindrops). Finally, snowfall at the surface can be composed of individual ice crystals, which may display uniform orientations, ice crystal aggregates (snowflakes), and near-spherical graupel particles that grow by collecting frozen cloud droplets in

convective updrafts like their larger hailstone relatives. Clearly, these principal precipitation-generating mechanisms should be easily separable on the basis of the LBDT.

The bright-band phenomenon warrants further examination. Shown in Fig. 6 and Plate 14.5 are vertical profiles of returned lidar and W-band radar power and depolarization (averaged over 2 min) and height–time displays of ruby lidar backscattering and depolarization obtained from light rainshowers. Note in Fig. 6 that with increasing height the nearly nondepolarizing raindrops (which have not yet reached the ground) give way to the much more strongly scattering and depolarizing snowflakes aloft. The rapid backscattering increase in the snow starts where severely melted snowflakes collapse into raindrops, but is soon followed by a rapid decrease in signal owing to the strong attenuation from the relatively large low-density snowflakes. Although model results have shown that the width and strength of the peak in snow backscattering above the melting layer depends on the precipitation intensity (Sassen, 1977b), the appearance of the signal on an oscilloscope display often resembles that of the microwave radar "bright band." Because the lidar "bright band" analog is related to the strong optical attenuation in snow, however, its cause is completely foreign to that at microwave frequencies, which results from dielectric effects in wet snowflakes. Finally, also note the conspicuous lidar "dark band" that separates the raindrops and snowflakes, which went unexplained until recently despite its dramatic appearance (Uthe, 1978).

As for the cause of this lidar dark band, Sassen and Chen (1995) offered an explanation of this phenomenon using ray optics theory combined with laboratory experiments of melting ice drops suspended in a laser beam (Sassen, 1977c). Lorenz–Mie theory dictates that water spheres backscatter light exclusively through surface waves and axial retroreflections that include contributions from both the front and the rear drop faces (Bryant and Cox, 1966). Laser experiments have also illustrated that the rear face reflection is a significant contributor to the total backscattering, because the front surface acts as a lens to focus light on the rear face (Ro *et al.*, 1968). However, an inhomogeneous raindrop behaves differently because the irregular ice core of a collapsed snowflake in effect blocks the internal paraxial return and so diminishes backscattering. It is clear then that a sudden increase in backscattering would occur as the melting process nears completion. Thus, the lidar dark band appears to owe its existence to two microphysical events in the melting zone: the structural collapse of the severely melted snowflake, which suddenly decreases laser backscattering owing to the combination of decreased particle cross sections and concentrations (from increased fall speeds), and the near completion of the melting process, which suddenly increases the returned power by allowing the full complement of spherical particle backscattering mechanisms to come into play.

The approximately 1-h height versus time display in Plate 14.5, however, indicates that the lidar-observed behavior of the melting region can be quite variable.

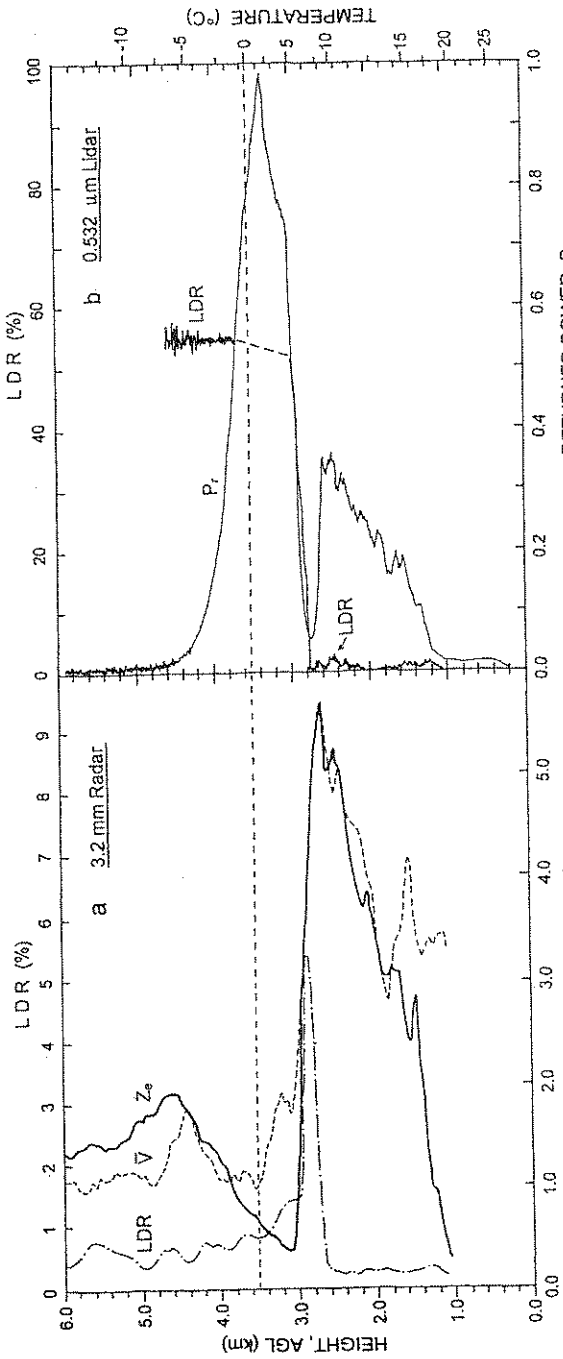

Figure 6 Comparison of vertical profiles of 3.2-mm microwave radar and 0.532-μm PDL data obtained from the melting layer, where LDR is the linear depolarization ratio, V the Doppler velocity, Z_e the radar reflectivity factor, and P_r the returned laser power in relative units. The lidar LDR data could not be calculated near the freezing level (dashed line) because of off-scale signals in the depolarized channel. Reprinted from K. Sassen and T. Chen (1995), The lidar dark band: An oddity of the radar bright band analogy, *Geophys. Res. Lett.* **22**, 3505–3508.

These zenith ruby lidar returned energy and depolarization displays depict the passage of a modest thunderstorm that briefly produced light rain at the FARS site around 2212 UTC. This storm was generated over the nearby Oquirrh Mountains during the summer monsoon season, and only brushed our location to yield a trace of rain, thus allowing the lidar to capture a cross section of the propagating convective shower. Initially, anvil layers up to 9 km and pendant mammatta structures were interrogated, but as the main thunderstorm anvil and precipitation advected over the site, the range of lidar probing was limited by the strong optical attenuation (seen from ~2200–2225). Note the sheared ice particle fall streak that descends from approximately 7 km at 2200 to 4 km at 2210, to be transformed below into a near-vertical rain shaft as a result of the higher raindrop fall speeds.

Although much of the cloud can be seen to produce typical 0.45–0.5 ice δ values, two notable exceptions are apparent. The first occurs between 6.5 and 7 km where low ratios occur in the anvil owing to the presence of horizontally oriented ice plates, as was confirmed by tilting the lidar a few degrees off the zenith at 2158:20. More notable is the depolarizing behavior of the particles in the melting zone, which show some surprising features in addition to the expected ice–water δ-value transition. The lidar dark band at 3.5 km separating the snow/rain regimes is particularly obvious from 2205 to 2215. However, note the absence of the dark band in the rain shafts after 2215, the wide range of depolarization in the rain varying from approximately 0 to 0.2, and the gap in the ice returns just above the rain around 2205. In this last respect this bright-band resembles more its microwave radar analog (a result of water/ice dielectric constant differences), in contrast to the melting layer study of Sassen and Chen (1995). It is obvious that understanding the bright band phenomena requires an improved characterization of the microphysics in the melting zone, including ice particle type (single crystals versus aggregates, graupel, or hail), and raindrop size and susceptibility to oscillate in response to turbulence and collisions. Such shape deformations could generate the relatively significant depolarization noted at about 2210 (Sassen, 1977c), or alternatively melting hailstones could have been responsible.

VIII. CONCLUSIONS AND OUTLOOK

We have attempted to illustrate here how lidars employing the backscatter depolarization technique have successfully exploited the sensitivity of light scattering to remotely determine the characteristics of nonspherical atmospheric particles. Starting in the early 1970s, the capabilities of polarization lidar for differentiating between the great range of atmospheric targets was comprehensively examined in the field and laboratory. Lidars operating at visible and near-infrared wavelengths sense depolarization arising from various sources: Rayleigh-scattering molecules, aerosols in the Rayleigh and Rayleigh–Mie transition zone,

and cloud and precipitation particles mostly in the geometric optics domain, which when present typically dominate the backscattered signal.

Polarization lidar studies of aerosols have made significant strides in analyzing the exotic clouds of the stratosphere, but relatively little has been accomplished with respect to the aerosols in the lower tropospheric boundary layer. The problems associated with the quantitative analysis of aerosol properties are numerous, but with the use of polarization diversity coupled with intrinsically calibrated lidar techniques such as Raman and HSRL, basic uncertainties can be overcome and attention focused on better understanding particle shape, size, and composition, taking into account humidity effects. We look forward to such lidar applications for the improved study of tropospheric aerosols.

As for large and nonabsorbing (relative to the laser wavelength) hydrometeors, the results gained early on (see, e.g., Fig. 2), along with ray-tracing theory, clearly imply that laser depolarization is sensitive to the exact shape of the hydrometeors. This is very unlike Rayleigh scattering, which essentially senses nonspherical particles as equivalent ellipsoids regardless of the presence of surface or internal structures. Rather, photons interact with every nook and cranny of a complex particle to a scale on the order of the incident wavelength. As reviewed in Sassen (1991), backscatter depolarization depends on the balance between the sums of nondepolarizing specular reflections and the internally refracted/reflected ray paths and intracrystal element scatterings responsible for depolarization. Take the example of a spatial dendritic-branched ice crystal: The 3D aspect promotes interbranched and internal scatterings characteristic of randomly oriented hexagonal particles, but at the same time, as such particles acquire frozen cloud droplets through the accretion process, each near hemisphere acts like a miniature diffusing element until in the limit, a graupel particle, very high δ values approaching the diffusing medium of ground glass are encountered.

As useful as polarization lidar measurements of clouds and aerosols have been, however, their utility for atmospheric research can be enhanced when the data are collected as part of a coordinated active and passive remote-sensing ensemble, often resulting in a striking synergy of observations. In addition to lidars, the ensemble currently in vogue includes short-wavelength Doppler radars, dual-channel microwave radiometers, and various visible and infrared radiometers. This multiple remote sensor approach has increased steadily in importance in field research programs, and as illustrated here, polarization lidar plays a crucial role in a number of applications. Most notably, polarization diversity allows for the unambiguous identification of liquid water clouds, the accurate determination of cloud base and (cirrus) cloud top heights, and a measure of the microphysical content of ice clouds and precipitation. This applies to lidars either on the ground or in high-flying aircraft (Spinhirne *et al.*, 1983), as well as potentially from Earth's orbit (Winker and Trepte, 1998). Modern lidar/radar "bright band" research is an excellent example of how fundamental scattering principles can be applied to

comprehending the intricacies of the hydrometeor phase change process. As a matter of fact, the induced scattering variations are so intriguing that a new feature, the lidar "dark band," was only recently recognized.

We look forward to the continued integration of polarization diversity into other lidar probing techniques for probing clouds, particularly those methods that effectively separate the molecular and cloud/aerosol backscattering constituents (Ansmann *et al.*, 1992). Not only will depolarization data enhance and improve the interpretation of cloud and aerosol quantities, but they can also be used as a quality check on the precision of some spectrally separated channels (e.g., "pure" molecular for which Rayleigh-predicted values of δ are known). The approach of using predictions from detailed cloud microphysical models to help evaluate lidar returns is clearly promising. We also believe that a more concerted focus given to evaluating additional laser backscatter methods such as circular depolarization and complete Stokes parameterization may contain unique, and as yet unknown attributes, particularly with regard to utilizing propagation effects for increasing our knowledge of hydrometeor content. The addition of polarization diversity is economical in terms of hardware and indispensable in terms of dealing with nonspherical atmospheric scatterers.

ACKNOWLEDGMENTS

Our recent polarization lidar research program has been funded by NSF Grant ATM-9528287, NASA Grants NAG-1-1314 and NAG-2-1106, and DOE Grant DEFG0394ER61747 from the Atmospheric Radiation Measurement program.

Chapter 15

Light Scattering and Radiative Transfer in Ice Crystal Clouds: Applications to Climate Research

K. N. Liou, Yoshihide Takano, and Ping Yang
Department of Atmospheric Sciences
University of California, Los Angeles
Los Angeles, California 90095

Light Scattering by Nonspherical Particles: Theory, Measurements, and Applications

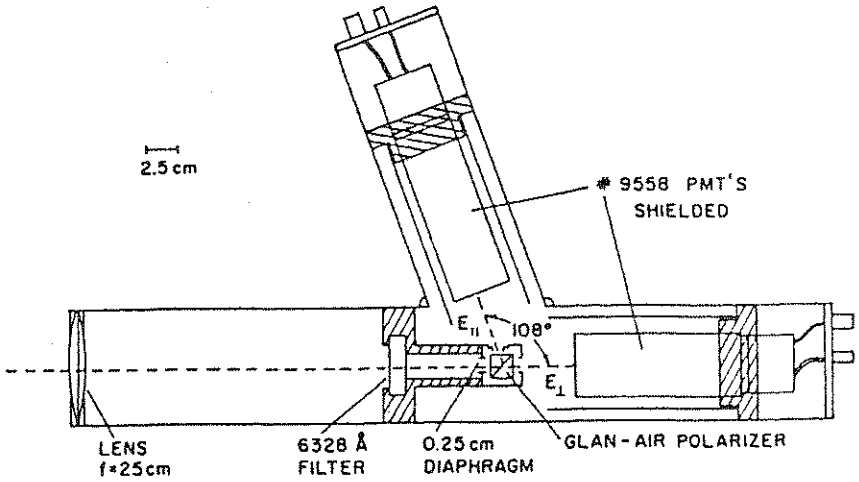

Figure 3 Typical polarization lidar receiver design using a polarizing prism and dual photomultiplier tube (PMT) detectors to permit simultaneous depolarization measurements. This example is for a laboratory lidar analog receiver, and so has a forward collecting lens. Reprinted from K. Sassen (1974), Depolarization of laser light backscattered by artificial clouds, *J. Appl. Meteorol.* **13**, 923–233. Copyright © 1974 American Meteorological Society.

of a dual-polarization receiver, in this case from a CW laser–lidar analog device (Sassen, 1974), which substitutes a light-collecting lens for the reflector used in pulsed lidar systems. The standard receiver components are a laser line interference filter (to block out background solar scattering), a field-of-view (FOV) limiting aperture and polarizer prism (in this case a Glan-air calcite cube) placed at the receiver focal point, and the dual detectors. In this example, two extended S-20 photomultiplier tubes were used to detect the backscattered 0.633-μm HeNe laser light. Although this design dates from the early 1970s, it remains in vogue today.

For polarization applications, the use of steering mirrors for directing the laser beam is unwise in order to avoid unnecessarily corrupting the transmitted and received polarization properties. Thus, polarization lidars usually involve placing the laser and telescope side by side on a stable table that is pointed into the vertical direction, after assuring the parallel alignment of the two beams. (Alternatively, a 45° mirror can be used to direct the beam into the receiver FOV.) Shown in Fig. 4 is a photograph of our turnkey ruby (0.694-μm) lidar system at the University of Utah Facility for Atmospheric Remote Sensing (FARS), which uses the receiver design of Fig. 3 and the side-by-side configuration on a (manually) steerable table supported by a yoke. The ability to steer the lidar is important to aid in beam alignment (with the use of a distant target board and steerable collimator), but also for allowing the collection of off-zenith measurements from ice clouds to

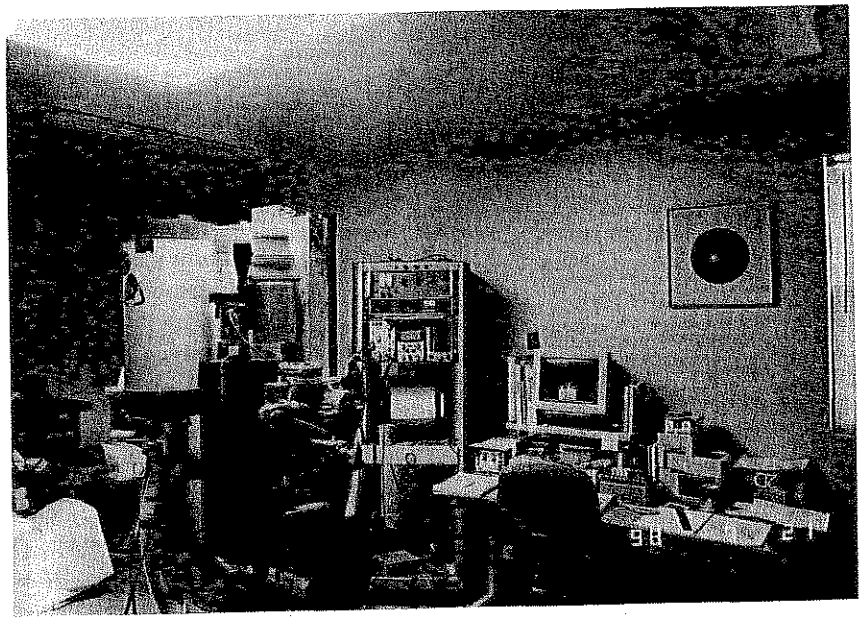

Figure 4 Photograph of a basic polarization lidar installation, at the University of Utah Facility for Atmospheric Remote Sensing. The PC-controller station is visible at right; at left are the laser transmitter, telescope receiver, and infrared radiometer units mounted on a table supported by a yoke to permit scanning.

identify anisotropic scattering conditions, as explained later. Note from Fig. 4 the placement of the collimator directly in front of the laser, and adjacent to it, the coaligned PRT-5 infrared radiometer. Data acquisition and storage for this system is accomplished simply, using a digital storage oscilloscope and a personal computer (PC) with 8-mm tape backup. This facility was built specifically for remote-sensing studies and has an opening skylight for the lidar and a roof parapet for mounting a variety of supporting radiometers and cameras.

The divergence of the laser beam and the FOV of the receiver defined by the aperture have important consequences for polarization data interpretation. Owing to the finiteness of these angles, the effects of laser pulse attenuation differ from that predicted by the Beer–Lambert law for an infinitely narrow divergence angle. This not only complicates quantitative data analysis for standard lidar systems, but also impacts on depolarization analysis through the viewing of multiply scattered radiation by the receiver. On the other hand, this aspect could be used to help interpret lidar signals when the FOV is rapidly changed. Other improvements could be the addition of multiwavelength depolarization measurements for

and polluted lower troposphere, particularly in conjunction with HSRL or Raman measurements to separate out the molecular constituents, hold particular promise for characterizing the content of such climatically important aerosols.

Boundary layer aerosol research is further complicated by the effects of relative humidity, which causes hygroscopic aerosols to deliquesce and swell into spherical haze particles. Such wetted particles may have solid inclusions and odd refractive indices, but will generate near-zero δ because of the relatively minute particle sizes. Thus, the δ values from hygroscopic particles will decrease as the relative humidity increases (Murayama *et al.*, 1997). As for the dry particulates, their depolarizing properties will depend on their size, composition (i.e., refractive index and uniformity), and shape (McNeil and Carswell, 1975; Kobayashi *et al.*, 1985, 1987). Because boundary layer aerosols may comprise a mixture of non- and hygroscopic particles of various materials over a large size range, particularly in urban areas, this scattering "soup" presents significant problems in quantitative lidar signal analysis, but polarization diversity in combination with spectroscopic techniques could be of great benefit.

Occasionally, dense (i.e., relative to molecular scattering) aerosol layers in the free troposphere are created by catastrophic local or regional events, such as fierce dust storms or fires. Plate 14.1 (see color Plates 14.1–14.5) shows an image of an Asian (Kosa) dust storm, as the particulates were swept up into a developing weather system and advected over a polarization lidar in Tokyo, Japan (Murayama *et al.*, 1998). Present in the returned energy display are sporadic strongly scattering cirrus clouds between 9 and 12 km, streaks of Kosa dust descending from approximately 11 km, and the aerosol of the boundary layer in the lowest kilometer. In terms of depolarization, the cirrus produced $\delta \approx 0.45$, the dust between 0.1 and 0.2, and the low-level aerosol less than 0.1. Note that the strongest returns in the boundary layer correspond to $\delta > 0.05$, which are regions of activated haze particles. In contrast, the significant depolarization in the Kosa dust, despite their relatively weak backscattering, indicates that they are crystalline particles. One may ask whether these potential cloud nuclei may have interacted with the cirrus clouds clearly embedded in the dust plume.

The example of a smoke plume created by a brush/forest fire approximately 25 km upwind of the FARS site in Plate 14.2 depicts a more dynamic microstructure in the dense aerosol cloud, which had a milky, bluish appearance. The layer is quite irregular, indicative of variations in the fire conditions that created the plume, and also perhaps preserving gravity waves. Toward the end of the display, a tongue of aerosols descends toward the surface (at 1.52 km above mean sea level, MSL) during a period of plume fumigation. The corresponding δ values decrease with height in the smoke layer: $\delta < 0.025$ are found at the layer top, whereas values up to 0.10 occur at the bottom, particularly near the end of the period. We conclude that the backscattering was dominated by spherical haze particles from condensed water and organic vapors in the upper regions of the layer, but that

relatively large and irregular ash particles were in the process of sedimenting out of the layer, perhaps aided by coagulation. Following these observations, a light coating of gray ash was noted on the lidar telescope window.

It is particularly with regard to researching the aerosols of the stratosphere that polarization lidar has played a leading role (Iwasaka and Hayashida, 1981). Because the distinction between stratospheric clouds and aerosols is sometimes vague, as the particles remain small in response to limited growth opportunities and rapid fallout in the thin air, we will consider both here. Principally, stratospheric scatterers can be divided into (i) the background aerosol dominated by (spherical) aqueous sulfuric acid droplets generated photochemically *in situ*; (ii) the apparently uncommon polar stratospheric clouds (PSCs) of various types often connected to ozone depletion; and (iii) the occasional volcanically injected aerosols composed of sulfuric acid droplets, ash, and possibly frozen particles. The major aerosol/cloud forming materials include compounds derived from sulfuric and nitric acids admixed with water, providing a rich tableau for theoretical chemists.

Spherical, homogeneous acid droplets must generate $\delta \approx 0$, and so are easily identified (Sassen and Horel, 1990). Frozen multisubstance particles, however, will depolarize visible laser light not only to the degree dictated by their amount of nonsphericity but also according to their size: Stratospheric particles tend to reside in the Rayleigh–Mie transition region with regard to light scattering. A number of theoretical studies have shown that variations in δ measured at a given wavelength are highly sensitive to the particle size parameter, which represents a significant complication to single-wavelength lidar analyses (Mishchenko and Sassen, 1998). Based largely on lidar studies, three distinct types of PSCs have been identified, although the question of the precise corresponding particle compositions has not been settled by theoretical chemists (Poole *et al.*, 1990). Recently, it has also been demonstrated that ice crystal clouds generating strong depolarization can also inhabit the Antarctic middle stratosphere (Gobbi *et al.*, 1998).

The fate of volcanically produced aerosols in the lower stratosphere (LS) and upper troposphere (UT) also involve chemical processes. Based on laboratory studies (Sassen *et al.*, 1989a), the neutralization and partial crystallization of sulfuric acid drops from the absorption of ammonia gas of lower-tropospheric origin was shown to generate $\delta \sim 0.1$ for micrometer-sized particles, which were similar to lidar measurements in an unusual volcanic aerosol layer injected into the UT over Central America and later studied over Salt Lake City, Utah (Sassen and Horel, 1990). Also unexpected were the δ values of approximately 0.05 measured in the LS following the 1991 Mt. Pinatubo volcanic eruptions at times of unusually cold midlatitude tropopause temperatures in conjunction with Bishop's ring observations (Sassen *et al.*, 1994a). It was conjectured that nonspherical submicrometer-sized frozen sulfuric acid tetrahydrate (SAT) particles could have been responsible for the optical display and nonzero δ values.

the potentially strong attenuation in the snowfall below, and of course may often go undetected with lidar if the attenuation is strong enough. Nonetheless, the versatility of the LBDT has been amply illustrated by lidar studies of orographic storm clouds. In addition to identifying liquid-dominated SLW and mixed-phase clouds, applying the principles of hydrometeor shape, surface complexity governing backscatter depolarization, and orientation allows the discrimination of graupel, rimed and pristine snowflakes, and uniformly oriented ice crystals. Such capabilities are important for cloud seeding research because the locations (and temperatures) of SLW clouds and the growth mechanism of precipitation particles are closely tied to the likelihood of the successful introduction of artificial ice nuclei.

VI. CIRRUS CLOUD RESEARCH

As demonstrated early on (Schotland *et al.*, 1971), the differences in δ between water and ice clouds were so dramatic that there was little doubt that cloud thermodynamic phase discrimination was inherent in the LBDT, which is quite important because such clouds at high altitudes have distinct radiative effects (Sassen *et al.*, 1985). This recognition came at a critical time, as it was becoming apparent that the extensive cirrus cloud layers, which covered a significant portion of the globe, would likely have a major impact on our climate and on how our atmosphere would respond to the hypothesized changes brought about by the buildup of greenhouse gases through cloud feedback mechanisms (Liou, 1986). The next step was to evaluate the information content of depolarization variations in ice clouds, and this effort gained impetus in the 1980s as scientific attention became focused on cirrus clouds in order to better understand their impact on the planet's radiation balance (Sassen *et al.*, 1990b). Ray-tracing theory has clearly demonstrated that δ values depend critically on the hexagonal ice crystal axis ratio (Takano, 1987; Takano and Liou, 1995) and that preferentially oriented crystals generate lidar elevation angle-dependent δ values (Takano and Jayaweera, 1985). For example, it can be seen from Table I that δ can vary from about 0.3 for randomly oriented thin plates to 0.6 for solid columns. In other words, δ increases with increasing axis ratio, and when the effects of the birefringence property of ice are also considered, the δ_b values in Table I tend to be somewhat stronger. Thus, according to theory, polarization lidar should have the capability of discriminating between basic ice crystal types. Experimental differences depending on crystal habit were also apparent in the field and laboratory (see the review in Sassen, 1991).

However, the situation in nature seems to have limited these laser remote-sensing opportunities, because most cirrus (off-zenith) measurements reveal δ in the 0.4–0.5 range. It appears that, as indicated by direct *in situ* particle sampling

Table I

Backscatter Linear Depolarization Ratio Values at Visible Wavelengths Computed Through Ray Tracing for Randomly Oriented Solid Ice Crystals with the Indicated Length L to Radius a Ratios (in μm). The Two Columns Show the Results Computed Ignoring (δ) and Including (δ_b) Ice Birefringence Effects

$L/2a$	δ	δ_b
8/80 (thin plate)	0.339	0.399
16/80 (plate)	0.355	0.396
32/80 (thick plate)	0.394	0.508
64/80 (short column)	0.382	0.500
200/80 (column)	0.550	0.616
400/80 (long column)	0.563	0.611

Source: Adapted from Takano (1987).

(Sassen *et al.*, 1994b), cirrus ice crystal collections often show a great diversity in particle habits and axis ratios reflecting dynamic cloud processes involving a combination of vertical redistribution (from vertical air motions and sedimentation), turbulent mixing, and new particle generation, as shown by two-dimensional (2D) model simulations (e.g., Khvorostyanov and Sassen, 1998). Thus, opportunities to probe homogeneous ice cloud compositions may be uncommon, although speculations as to the content of particular regions of cirrus clouds have been widespread. For example, in Sassen *et al.* (1989b), regions associated with Doppler radar-detected updrafts yielded rather low δ (~0.2–0.3), which were attributed either to rapidly growing haze particles, as precursors to new ice particles, or to the peculiar shapes of newly formed ice crystals. Atypically high δ (~0.5–0.8) were measured at the tops of unusually cold, corona-producing mid-latitude cirrus layers extending slightly into the LS and also in contact with tropopause folds (Sassen *et al.*, 1995). These high δ values were attributed to the effects on ice particle nucleation and growth of homogeneously frozen sulfuric acid droplets of stratospheric/volcanic origin. Recently, *in situ* sampling of a cold corona-producing cirrus layer (Sassen *et al.*, 1998) revealed the presence of small (~20 μm diameter) simple ice crystals, but the question of the high-δ particle shape has not yet been fully resolved.

Microphysically, a ubiquitous ice cloud polarization lidar application deals with the anisotropic scattering behavior of horizontally oriented planar ice crystals, which initially led to the misidentification of an ice altostratus layer as mixed phase using zenith lidar (Platt, 1977), but soon offered promise in understanding the fall attitudes of atmospheric ice plates (Platt, 1978; Platt *et al.*, 1978). Because

convective updrafts like their larger hailstone relatives. Clearly, these principal precipitation-generating mechanisms should be easily separable on the basis of the LBDT.

The bright-band phenomenon warrants further examination. Shown in Fig. 6 and Plate 14.5 are vertical profiles of returned lidar and W-band radar power and depolarization (averaged over 2 min) and height–time displays of ruby lidar backscattering and depolarization obtained from light rainshowers. Note in Fig. 6 that with increasing height the nearly nondepolarizing raindrops (which have not yet reached the ground) give way to the much more strongly scattering and depolarizing snowflakes aloft. The rapid backscattering increase in the snow starts where severely melted snowflakes collapse into raindrops, but is soon followed by a rapid decrease in signal owing to the strong attenuation from the relatively large low-density snowflakes. Although model results have shown that the width and strength of the peak in snow backscattering above the melting layer depends on the precipitation intensity (Sassen, 1977b), the appearance of the signal on an oscilloscope display often resembles that of the microwave radar "bright band." Because the lidar "bright band" analog is related to the strong optical attenuation in snow, however, its cause is completely foreign to that at microwave frequencies, which results from dielectric effects in wet snowflakes. Finally, also note the conspicuous lidar "dark band" that separates the raindrops and snowflakes, which went unexplained until recently despite its dramatic appearance (Uthe, 1978).

As for the cause of this lidar dark band, Sassen and Chen (1995) offered an explanation of this phenomenon using ray optics theory combined with laboratory experiments of melting ice drops suspended in a laser beam (Sassen, 1977c). Lorenz–Mie theory dictates that water spheres backscatter light exclusively through surface waves and axial retroreflections that include contributions from both the front and the rear drop faces (Bryant and Cox, 1966). Laser experiments have also illustrated that the rear face reflection is a significant contributor to the total backscattering, because the front surface acts as a lens to focus light on the rear face (Ro *et al.*, 1968). However, an inhomogeneous raindrop behaves differently because the irregular ice core of a collapsed snowflake in effect blocks the internal paraxial return and so diminishes backscattering. It is clear then that a sudden increase in backscattering would occur as the melting process nears completion. Thus, the lidar dark band appears to owe its existence to two microphysical events in the melting zone: the structural collapse of the severely melted snowflake, which suddenly decreases laser backscattering owing to the combination of decreased particle cross sections and concentrations (from increased fall speeds), and the near completion of the melting process, which suddenly increases the returned power by allowing the full complement of spherical particle backscattering mechanisms to come into play.

The approximately 1-h height versus time display in Plate 14.5, however, indicates that the lidar-observed behavior of the melting region can be quite variable.

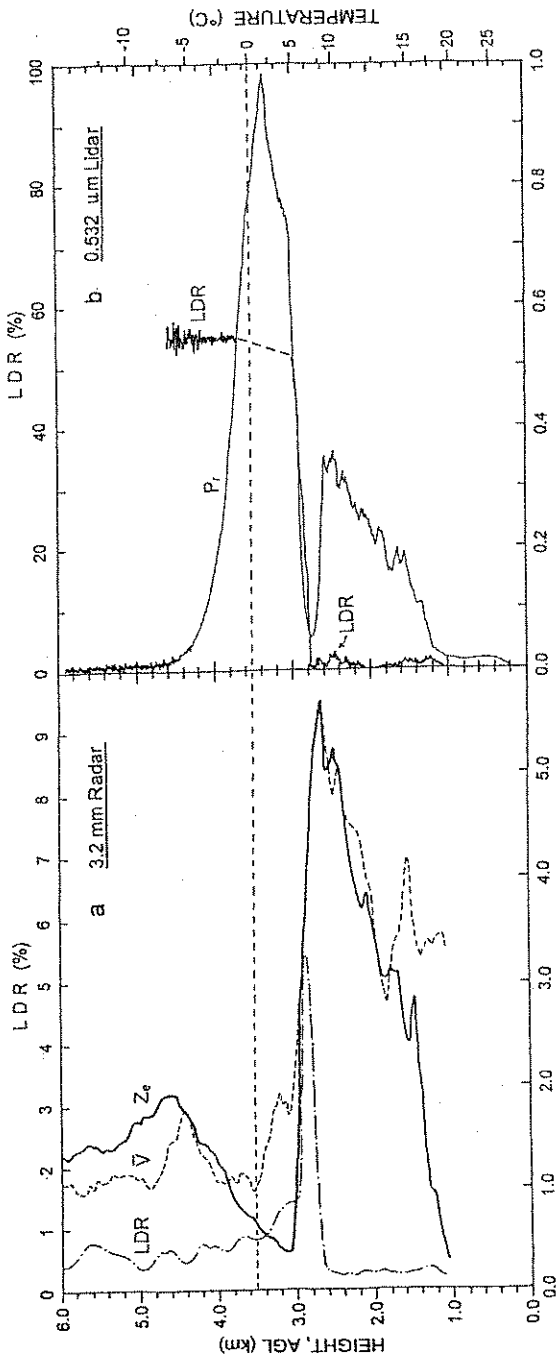

Figure 6 Comparison of vertical profiles of 3.2-mm microwave radar and 0.532-μm PDL data obtained from the melting layer, where LDR is the linear depolarization ratio, V the Doppler velocity, Z_e the radar reflectivity factor, and P_r the returned laser power in relative units. The lidar LDR data could not be calculated near the freezing level (dashed line) because of off-scale signals in the depolarized channel. Reprinted from K. Sassen and T. Chen (1995), The lidar dark band: An oddity of the radar bright band analogy, *Geophys. Res. Lett.* **22**, 3505–3508.

comprehending the intricacies of the hydrometeor phase change process. As a matter of fact, the induced scattering variations are so intriguing that a new feature, the lidar "dark band," was only recently recognized.

We look forward to the continued integration of polarization diversity into other lidar probing techniques for probing clouds, particularly those methods that effectively separate the molecular and cloud/aerosol backscattering constituents (Ansmann *et al.*, 1992). Not only will depolarization data enhance and improve the interpretation of cloud and aerosol quantities, but they can also be used as a quality check on the precision of some spectrally separated channels (e.g., "pure" molecular for which Rayleigh-predicted values of δ are known). The approach of using predictions from detailed cloud microphysical models to help evaluate lidar returns is clearly promising. We also believe that a more concerted focus given to evaluating additional laser backscatter methods such as circular depolarization and complete Stokes parameterization may contain unique, and as yet unknown attributes, particularly with regard to utilizing propagation effects for increasing our knowledge of hydrometeor content. The addition of polarization diversity is economical in terms of hardware and indispensable in terms of dealing with nonspherical atmospheric scatterers.

ACKNOWLEDGMENTS

Our recent polarization lidar research program has been funded by NSF Grant ATM-9528287, NASA Grants NAG-1-1314 and NAG-2-1106, and DOE Grant DEFG0394ER61747 from the Atmospheric Radiation Measurement program.

Chapter 15

Light Scattering and Radiative Transfer in Ice Crystal Clouds: Applications to Climate Research

K. N. Liou, Yoshihide Takano, and Ping Yang

Department of Atmospheric Sciences
University of California, Los Angeles
Los Angeles, California 90095

Light Scattering by Nonspherical Particles: Theory, Measurements, and Applications

Chapter 17

Microwave Scattering by Precipitation

Jeffrey L. Haferman
Fleet Numerical Meteorology and Oceanography Center
Monterey, California 93943

Light Scattering by Nonspherical Particles: Theory, Measurements, and Applications

I. INTRODUCTION

Because microwaves readily penetrate clouds and do not depend on the sun as a source of illumination, microwave radiometry provides an excellent compliment to infrared and visible remote-sensing techniques. In contrast to *active* microwave remote sensing (Chapter 16) in which a pulse is *actively* emitted from a source and then backscattered from a target, *passive* microwave radiometers measure radiation that is naturally emitted by some source, such as the atmosphere and surface of Earth. This naturally emitted radiation may interact with other matter and be scattered, absorbed, and reemitted before being detected by a radiometer. In this chapter, microwave scattering by nonspherical hydrometeors will be discussed in the context of remote sensing of precipitation.

The potential of using passive microwave radiometry for observing precipitation from space was first explored mathematically by Buettner (1963) over three decades ago. In 1972, the first Electrically Scanning Microwave Radiometer (ESMR) was launched aboard *Nimbus-5*, and some of the first spaceborne passive microwave precipitation retrievals were performed. Soon thereafter, passive microwave precipitation observations were made using radiometers aboard *Skylab* in 1973, the *Nimbus-6* ESMR in 1975, and the Scanning Multichannel Microwave Radiometer (SMMR) aboard *Nimbus-7* and *Seasat-1* in 1978.

Since these early missions, several projects dedicated to the accurate measurement of global precipitation have been developed. For example, the first Special Sensor Microwave/Imager (SSM/I) was launched in June 1987 as part of the Defense Meteorological Satellite Program. Another project, the Global Precipitation Climatology Project established by the World Climate Research Program, was created to produce monthly global rainfall totals on a 2.5° latitude by 2.5° longitude scale for the period 1986–95 using data returned from satellite observations. In November 1997 the Tropical Rainfall Measuring Mission (TRMM) satellite was launched as part of a joint program between the United States and Japan to measure rainfall from space (Simpson *et al.*, 1996).

Some satellite methods of precipitation estimation use visible or infrared measurements to infer rainfall amounts. However, at these frequencies, the radiation observed by satellite radiometers originates from cloud tops and, therefore, is an indirect observation of the precipitation below. In contrast, measurements using microwaves that can penetrate clouds provide a more direct means of observing and estimating precipitation. To derive a mathematical relationship between the radiation measured by a satellite radiometer and the underlying precipitation structure, physically based microwave rainfall retrieval algorithms typically apply radiative transfer theory to microphysical cloud models to obtain brightness temperature (T_B) versus rain rate (R) relationships. In terms of the four-component Stokes intensity vector introduced in Section XII of Chapter 1, the brightness temperature is defined as the equivalent blackbody temperature of a

given Stokes intensity vector component. Current and past sensors have measured brightness temperatures at two orthogonal polarizations; future sensors may (and some current airborne sensors do) include polarimetric channels to measure the third (plane of polarization) and possibly the fourth (ellipticity) Stokes parameters (see Gasster and Flaming, 1998; Yueh, 1997).

Mathematically, the brightness temperature for the first Stokes parameter is obtained by inverting Planck's law for a fixed wavelength λ to yield

$$T_{B,I}(\vartheta, \varphi) = \frac{C_2}{\lambda \ln[1 + C_1/\{\lambda^5 |I(\vartheta, \varphi)|\}]} \operatorname{sgn}[I(\vartheta, \varphi)], \tag{1}$$

where $C_1 = 3.74126 \times 10^8$ W μm^4 m^{-2}, $C_2 = 1.4388 \times 10^4$ μm K, and I is the radiant intensity propagating in the direction described by the polar and azimuthal angles ϑ and φ.[1] The function sgn(x) is equal to 1 when its argument is positive, equal to 0 when its argument is 0, and equal to -1 when its argument is negative. Brightness temperatures for the other Stokes parameters (Q, U, and V) are obtained by switching the symbol I with the symbol for the Stokes parameter under consideration. Brightness temperatures for vertical and horizontal polarizations (Section III of Chapter 1) are obtained by first defining the alternate Stokes parameters

$$I_v = \frac{I + Q}{2}, \tag{2}$$

$$I_h = \frac{I - Q}{2}, \tag{3}$$

and then inserting I_v or I_h into Eq. (1) to obtain $T_{B,v}$ or $T_{B,h}$, respectively, where lowercase subscripts have been used to avoid confusion between vertically polarized brightness temperatures ("v") and the fourth Stokes parameter brightness temperature ("V").

Panegrossi *et al.* (1998) have noted that there is often a lack of consistency between model-generated T_Bs and those observed by actual satellite radiometers. They suggest that some of this mismatch may be attributed to (1) using one-dimensional radiative transfer models that do not account for three-dimensional precipitation structures and (2) approximating all hydrometeor species as spherical scatterers. Currently, it is not entirely clear how important these two issues are in terms of retrieving accurate precipitation quantities from satellite-based microwave radiometers. The three-dimensional issue has received some attention (e.g., Roberti *et al.*, 1994) throughout the years, but is still an outstanding problem. The assumption of spherical scatterers has also received some attention in

[1]The constants C_1 and C_2 are defined as $C_1 = 2\pi h c_0^2$ and $C_2 = hc_0/k$, where c_0 is the speed of light in a vacuum, h is Planck's constant, and k is the Boltzmann constant. In some literature, the constant C_1 is defined as hc_0^2.

the passive microwave remote-sensing literature, but, even though the theory is well known (Tsang *et al.*, 1985), it is not entirely clear how the assumption of sphericity impacts microwave precipitation retrievals.

The purpose of this chapter is to review the relevant literature that deals with the effect of nonspherical randomly and nonrandomly oriented hydrometeors on microwave brightness temperatures and to review the mathematical theory necessary to model scattering by nonspherical hydrometeors in passive microwave precipitation retrieval. It is known that small raindrops are nearly spherical, but as raindrop size increases, the shape can depart significantly from spherical (Chuang and Beard, 1990). Ice in the atmosphere can take on a variety of shapes and orientations (Pruppacher and Klett, 1997; Matson and Huggins, 1980). Thus, although no attempt is made here to quantify the effect of nonsphericity on passive microwave precipitation retrieval, it is hoped that the review presented will allow interested researchers to pursue this issue on their own.

Because some researchers have speculated that hydrometeor shape influences microwave polarization signatures, this issue is also touched upon. For example, Spencer *et al.* (1989) observed polarization differences[2] of about 5–10 K at the 85-GHz frequency of the SSM/I near convective cores over land and speculated that they were due to oriented ice within stratiform precipitation areas. Heymsfield and Fulton (1994a, b) noted SSM/I 85-GHz polarization differences between 8 and 13 K and 37-GHz polarization signatures up to 7 K in mesoscale convective systems and in tornadic storms over land. Petty and Turk (1996) observed similar 85-GHz signatures in moderate to heavy precipitation in tropical cyclones over the ocean. These authors attributed the polarization signatures to nonspherical hydrometeors with a preferred orientation and proposed that this only happens in stratiform-type precipitation (for convective precipitation, convective motion produces random orientation and larger, nearly spherical graupel particles, presumably leading to smaller polarization signatures). In addition, Kutuza *et al.* (1998) have observed large polarization signatures for downwelling microwave radiation propagating through precipitation.

The chapter is organized as follows. Section II reviews previous work in microwave radiative transfer modeling of nonspherical hydrometeors. Section III discusses the mathematical formulation for performing microwave radiative transfer calculations with nonspherical hydrometeors. Section IV describes a simple atmospheric model containing nonspherical hydrometeors and presents some microwave radiative transfer results for this model atmosphere. Finally, in Section V, conclusions and suggestions for future work are given.

[2]The terms "polarization difference" and "polarization signature" are taken throughout the text to mean the difference between vertically and horizontally polarized brightness temperatures, that is, $T_{B,v} - T_{B,h}$ $(= T_{B,Q})$.

II. REVIEW OF PREVIOUS WORK

A. Overview

The intent of this section is to present an overview of previous work done in the area of scattering by nonspherical hydrometeors in passive microwave precipitation retrieval studies. The following studies have been performed within the last couple of decades and are reviewed here to provide a framework for understanding the developments and the state of the art in this area. The following sections are organized according to a common author (not necessarily the lead author) of a set of papers. Some of the older studies (e.g., Oguchi, 1960) are not reviewed, but the interested reader may piece together a more complete historical account by referring to the citations in the studies reviewed here.

B. Weinman

1. Wu and Weinman (1984)

Wu and Weinman (1984) presented results showing upwelling[3] brightness temperatures at a zenith viewing angle of 50° for two orthogonal polarizations and using nonspherical particles for frequencies of 6.6, 10.7, 18, 21, and 37 GHz. They modeled polydispersions of oblate water drops and oriented oblate ice particles, over both water and land surfaces. The scalar form of the radiative transfer equation was solved by using the Eddington approximation for each polarization state. That is, horizontal and vertical extinction coefficients were defined and the radiative transfer equation was solved separately for each polarization. A linear anisotropic phase function defined by a polarization-independent asymmetry parameter was used, and the polarized extinction coefficients of the particles were computed for an angle of 50° with respect to the particle semi-minor axis of symmetry. To approximate an optically smooth ocean surface, a constant emittance value of 0.333 was used for horizontal polarizations, and a value of 0.605 was used for vertical polarizations. Over land, the surface was modeled as a Lambertian surface (see Section III.I) with an emittance of 0.9.

Despite the lack of rigor used in the formulation of the radiative transfer equation, several important observations were made by Wu and Weinman concerning the effect of hydrometeor shape on the computed upwelling brightness temperatures. First, spherical particles depolarize the strongly polarized signature emitted

[3]The term "upwelling brightness temperature" is taken throughout the text to mean the brightness temperature that represents the net radiation emitted in an upward direction by the entire atmospheric path between the ground and the observation point in the direction under consideration. "Downward brightness temperature" is defined as the net radiation emitted in a downward direction from a semi-infinite atmosphere along a given line of sight to an observation point on the ground.

by an optically smooth ocean surface. The amount of depolarization increases with frequency and with rain rate. For example, at 6.6 GHz and rain rates of 32 and 64 mm/h, the polarization difference is about 28.5 and 7.5 K, respectively, while at 37 GHz the polarization differences are 6.6 and 0.6 K at rain rates of 2 and 4 mm/h, respectively, and no polarization difference occurs for higher rain rates. Over land, the signal is unpolarized for all frequencies and rain rates.

Second, for spherical ice and nonspherical water drops, the signal over land becomes slightly polarized (less than 1 K for all frequencies and rain rates). Over water, the signal becomes depolarized as for the case of spherical hydrometeors, but never becomes completely depolarized for the range of frequencies (6.6–37 GHz) and rain rates (2–64 mm/h) considered. For example, at 37 GHz the polarization differences are about 1 K for rain rates between 4 and 16 mm/h. However, this can be considered to be an almost negligible effect on the polarization signal.

Third, and most significantly, deforming the ice hydrometeors (from spheres to spheroids) had the largest impact on upwelling polarization signatures over land and water. For example, at 37 GHz and rain rates in excess of 48 mm/h, the polarization signal was about 11 K. The polarization signal decreases monotonically as frequency decreases (about 6 K at 21 GHz and rain rates greater than 32 mm/h).

2. Kummerow and Weinman (1988)

Kummerow and Weinman (1988) used the T-matrix method to compute the extinction coefficients of polydispersions of horizontally oriented oblate ice and raindrops with an incidence angle of 50° with respect to the particle semi-minor axis. The frequencies considered were 10.7, 18, 37, 50.3, and 85.6 GHz. Unfortunately, no radiative transfer computations were performed. However, the extinction coefficients were parameterized as a function of rain rate via

$$k_e \left[\mathrm{km}^{-1}\right] = \kappa_1 R^{\kappa_2 + \kappa_3 \ln R}, \tag{4}$$

where k_e is a scalar extinction coefficient, $k_{e,v} = n_0[K_{11} + K_{22}]/2$ or $k_{e,h} = n_0[K_{11} - K_{22}]/2$, n_0 is the particle number density (see Chapter 1, Section VIII), and R is the rain rate in millimeters per hour. Values of κ_1, κ_2, and κ_3 were presented for liquid water and ice for the aforementioned frequencies.

The authors found that the horizontally polarized extinction coefficients were always larger than those for vertical polarization, but explained that this is because the hydrometeors were oriented with their long axis in horizontal alignment. An important finding from this study was demonstrated in a figure depicting the differences between the extinction coefficients of oblate spheroids and spheres of equal volume for horizontally and vertically polarized radiation as a function of rainfall rate for 18, 37, and 85 GHz. The figure showed that the horizontal

(vertical) extinction coefficients for oblate particles are larger (smaller) than the extinction coefficients for spherical particles and that the differences grow with frequency and rainfall rate. For intermediate rainfall rates (10–50 mm/h) the absolute differences are between about 0.02 and 0.07 km^{-1} for 85 GHz and between about 0.005 and 0.03 km^{-1} for 37 GHz.

3. Schols *et al.* (1997)

Schols *et al.* (1997) performed vector radiative transfer computations on a model atmosphere that contained spherical rain and oriented oblate snow and melting particles. Upwelling brightness temperatures and polarization differences were computed for a frequency of 85 GHz and a 53° viewing angle. The results demonstrated that the melting particles elevated 85-GHz brightness temperatures in comparison to results that excluded melting particles, and that the oriented ice particles created a polarization signature. The model results were consistent with observations over a stratiform rain event.

C. Evans

1. Evans and Vivekanandan (1990)

This study presented a simulation of radar and radiometer remote sensing of nonspherical atmospheric ice crystals. The study was geared toward the remote sensing of cirrus cloud properties, and the radiometric simulations were performed at frequencies of 37, 85, and 157 GHz. The discrete dipole approximation (DDA; see Chapter 5) was used to compute the radiative properties of horizontally oriented ice modeled as polydispersions of hexagonal plates, columns, and needles. These radiative properties were used as input to a vector radiative transfer model based on the adding–doubling method (Evans and Stephens, 1991). It was shown that, in general, ice particles of all shapes depress brightness temperatures (compared to the cases without ice) for all viewing angles at these frequencies, though the depression increases with frequency.

Some results from this study are shown in Figs. 1 and 2. Figure 1 shows the upwelling brightness temperature $T_{B,I}$ and polarization difference $T_{B,Q}$ as functions of zenith angle for 85 and 157 GHz and contrasts the base case (plates with density 0.92 $\mathrm{g/cm}^3$ and polydispersion maximum size of 2 mm) with a low particle density (0.23 $\mathrm{g/cm}^3$) case and lower maximum size (1 mm) case. All computations were performed using a three-layer atmosphere over a Lambertian surface (thus, polarization signatures are due to particle scattering only and not to surface effects). The figure shows the strong dependence of the brightness temperature depression on particle density and maximum size in the polydispersion. The po-

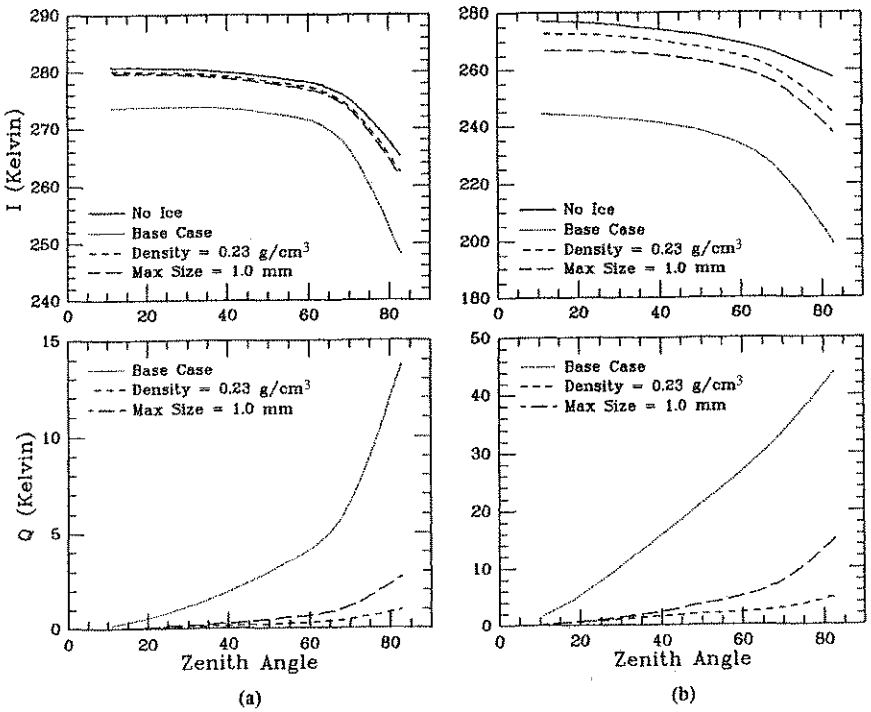

Figure 1 Upwelling brightness temperature $T_{B,I}$ and polarization difference $T_{B,Q}$ as functions of zenith angle for (a) 85 GHz and (b) 157 GHz. The base case (plates with density 0.92 g/cm^3 and polydispersion maximum size of 2 mm) are contrasted with a low particle density (0.23 g/cm^3) case and lower maximum size (1 mm) case. Reprinted from K. F. Evans and J. Vivekanandan (1990), Multiparameter radar and microwave radiative transfer modeling of nonspherical atmospheric ice particles, *IEEE Trans. Geosci. Remote Sens.* **28**, 423–437 (© 1990 IEEE).

larization difference $T_{B,Q}$ increases with bulk ice density, maximum particle size, frequency, and viewing angle. The polarization difference increases with viewing angle because the particles are oriented in the horizontal plane and the path length is longer. Finally, $T_{B,Q}$ is always positive, indicating that the horizontally polarized radiation is being scattered out of the viewing direction, leaving more vertically polarized radiation.

Figure 2 shows the effect of ice particle shape on upwelling brightness temperature and polarization difference as a function of zenith angle for frequencies of 85 and 157 GHz. The total ice mass for each case is 0.1 g/m^3, but the volume of the largest ice columns (with maximum dimension of 2 mm) is twice that of plates and 20 times that of needles. As shown in Fig. 2, the brightness temperature depression corresponds directly with the volume, with the more voluminous particles (columns, then plates, then needles) creating the largest depression.

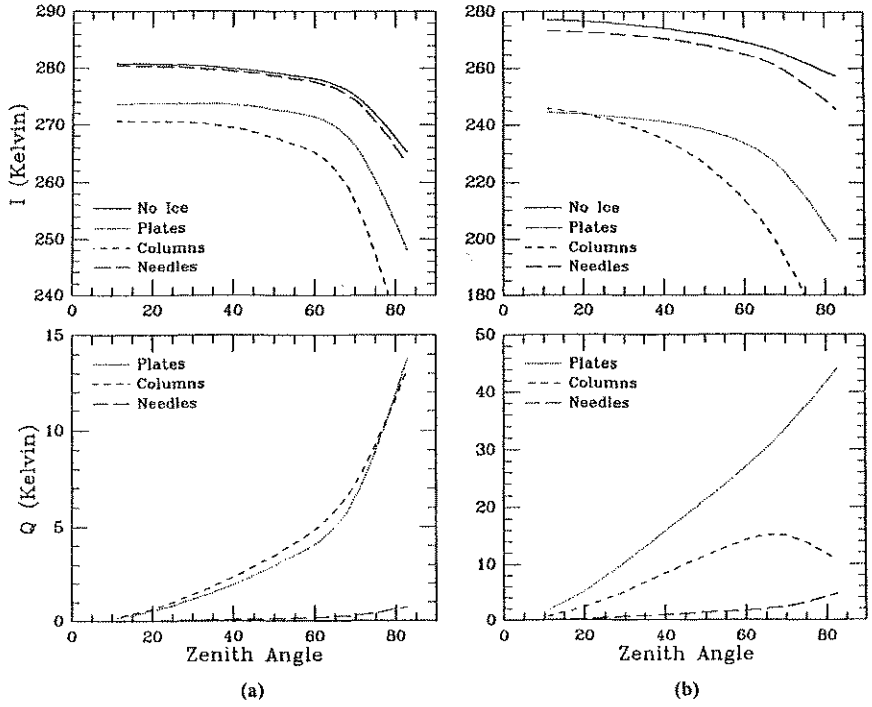

Figure 2 Upwelling brightness temperature $T_{B,I}$ and polarization difference $T_{B,Q}$ as functions of zenith angle for plates, columns, needles, and no ice layer: (a) 85 GHz and (b) 157 GHz. Reprinted from K. F. Evans and J. Vivekanandan (1990), Multiparameter radar and microwave radiative transfer modeling of nonspherical atmospheric ice particles, *IEEE Trans. Geosci. Remote Sens.* **28**, 423–437 (© 1990 IEEE).

2. Evans and Stephens (1995a, b)

Part I of this study (Evans and Stephens, 1995a) used the DDA to compute the single-scattering properties of five shapes of ice (solid and hollow columns, hexagonal plates, planar bullet rosettes, and spheres) at frequencies of 85.5, 157, 220, and 340 GHz. The large dimension of the particles ranged in size from 30 to 2000 μm, and the radiative properties of the polydispersion were computed using 18 different gamma size distributions (specified by characteristic particle size and

distribution width) over these particles sizes. The long axes of the ice particles were assumed to be randomly oriented in the horizontal plane, and the particle aspect ratios varied according to empirical formulas.

Many important findings were presented in this paper. First, it was noted that, for the frequencies considered, there are three regimes for extinction as a function of particle volume: (i) Absorption dominates and varies as particle volume; (ii) Rayleigh scattering dominates varying as the square of the volume; and (iii) beyond the Rayleigh regime scattering increases more slowly than the square of the particle volume.

A second finding was that, for a given particle shape, the characteristic particle size of the distribution L_m (defined as the median of the distribution of the dimension L to the third power, where L is the particle maximum size) is important in determining the extinction properties of the distribution. Finally, it was found that particle shape also has a significant effect on polarization: Plates were found to be the most polarizing shape, followed by planar rosettes and then columns.

The scattering quantities were also fit as functions of particle size for several incident angles. Part II of the study (Evans and Stephens, 1995b) used these quantities as input to a radiative transfer model to examine the sensitivity of upwelling brightness temperature depressions at nadir and 49° as a function of ice water path. More recently, Evans *et al.* (1998) have used the DDA and polarized radiative transfer modeling to lay the theoretical foundations for cirrus property retrievals.

D. Turk

1. Turk and Vivekanandan (1995)

Turk and Vivekanandan (1995) performed microwave radiative transfer simulations by considering oriented ice plates, oblate raindrops, and conical graupel, over both ocean and land surfaces. Results were presented for both upwelling and downwelling viewing angles, for frequencies of 10, 20, 37, and 85 GHz.

Some of the results obtained in this study are shown in Fig. 3, which illustrates the behavior of the upwelling brightness temperature as a function of viewing angle for the case of a 4-km-thick layer of oblate raindrops with a constant rain rate of 5 mm/h, underlying a 4-km layer of conical graupel, all over the ocean, for frequencies of 20, 37, and 85 GHz. The effect of the graupel layer becomes more pronounced as frequency increases: At 20 GHz, the addition of the graupel layer is nearly negligible, but at 37 and 85 GHz, the graupel layer depresses the brightness temperatures considerably relative to the graupel-free cases. For all frequencies, the polarization difference can be quite large for off-nadir viewing angles. For example, at 85 GHz, the polarization difference $T_{B,Q}$ is about +20 K

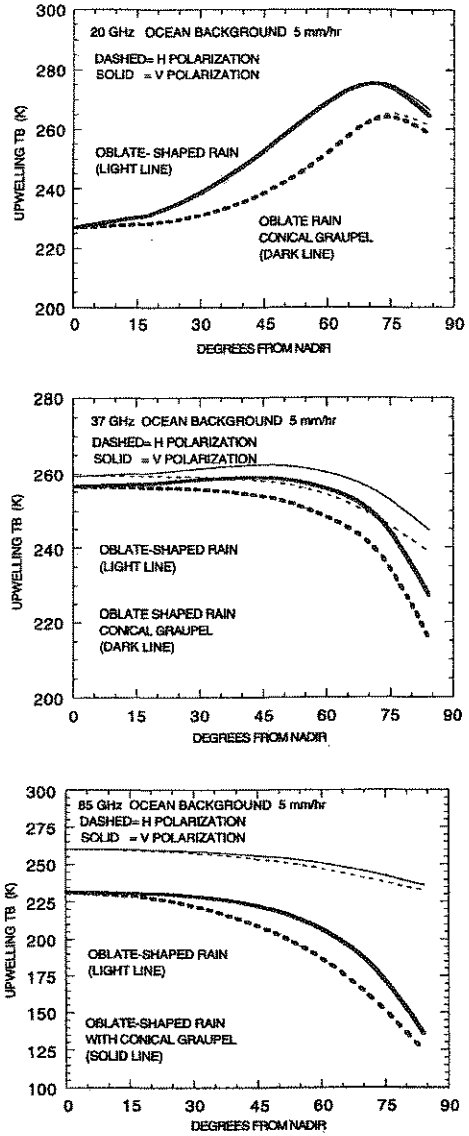

Figure 3 Upwelling brightness temperatures $T_{B,v}$ and $T_{B,h}$ at 20, 37, and 85 GHz as a function of view angle away from nadir. The thick curves denote a model consisting of a 4-km, 5-mm/h oblate spheroidally shaped rain layer beneath a 4-km layer of conical shaped graupel, and the thin curves denote a model consisting of a 4-km oblate rain layer only. Reprinted from J. Turk and J. Vivekanandan (1995), Effects of hydrometeor shape and orientation upon passive microwave brightness temperature measurements, *in* "Microwave Radiometry and Remote Sensing of the Environment" (D. Solomini, Ed.), pp. 187–196, VSP, Zeist, The Netherlands.

for viewing angles between 45° and 60°. For a fixed viewing angle of 48° (results not shown), the authors found polarization differences of about 20 K at 37 and 85 GHz for rain rates greater than 10 mm/h.

The authors also examined downwelling radiation at the surface and found that for a frequency of 85 GHz, the net downwelling brightness temperatures warmed with increasing ice plate mass content because of backscattering of the atmosphere and surface into the radiometer field of view. The polarization difference was found to be negative and had values of as much as −25 K for viewing angles between 45° and 60° from nadir. Computations at lower frequencies did not show these large polarization differences or brightness temperature warming because of the smaller albedo of ice at these frequencies. The results were also somewhat sensitive to the amount of cloud liquid water in the atmosphere.

2. Petty and Turk (1996)

This study used the model of Turk and Vivekanandan (1995) and compared the results to observed SSM/I brightness temperatures. The observed brightness temperatures were for situations corresponding to widespread, moderate to heavy rainfall in tropical cyclones. In general, the model results tended to overemphasize the polarization effects, though in many cases, the correct trends were produced. Furthermore, the observed SSM/I polarization signatures for rain rates between 5 and 50 mm/h (i) decreased linearly from about +10 K to 0 K at 19 GHz (presumably this is due to masking of the polarized surface as the atmosphere becomes opaque); (ii) were fairly constant with a mean value of +3.2 K for 37 GHz (this appears to be due to the scattering properties of the hydrometeors); and (iii) had values ranging from between +5 and +10 K for 85 GHz (again due to scattering by hydrometeors) in moderately scattering stratiform precipitation, and decreasing for more intensely scattering convective precipitation.

E. Liu

1. Liu *et al.* (1996b)

Apparently, the first fully three-dimensional polarized microwave code was developed by Liu *et al.* (1996b). The code combines forward and backward Monte Carlo techniques to solve the radiative transfer equation. Though the scheme does allow for the treatment of polarized radiation, it requires that the extinction matrix be diagonal, and, thus, it is not capable of modeling oriented particles, though it is capable of handling randomly oriented axisymmetric particles (Q. Liu, personal communication). This particular study considers only spherical particles and places emphasis on three-dimensional effects rather than concentrating on vector radiative transfer and polarization effects.

2. Liu and Simmer (1996)

This paper explored theoretically the effect of neglecting the vector radiative transfer approach when computing upwelling microwave brightness temperatures in the presence of spherical hydrometeors. The successive orders of scattering method was used for one-dimensional vector radiative transfer computations, and the Monte Carlo method (Liu *et al.*, 1996b) was used for three-dimensional vector radiative transfer computations. Though the formulation presented applies to randomly oriented axisymmetric particles (spheres, spheroids, ellipsoids, etc.), the findings of this study apply strictly to spherical particles. The formulation does not apply to preferentially oriented particles.

An important finding of this study applies to a homogeneous plane-parallel atmosphere with thermal sources and containing spherical particles. The finding is for polarized radiation emerging in an upward direction at the top of the atmosphere and is stated in terms of the phase matrix element Z_{21} (see Section VI of Chapter 1) as

$$Q \geq 0, \quad \text{when } Z_{21} \leq 0 \text{ for all scattering angles,} \tag{5}$$

$$Q \leq 0, \quad \text{when } Z_{21} \geq 0 \text{ for all scattering angles,} \tag{6}$$

$$Q = 0, \quad \text{when } Z_{21} = 0 \text{ for all scattering angles.} \tag{7}$$

If the preceding relations are only satisfied for some scattering angles, then the sign of Q depends on the single-scattering albedo, optical depth, and viewing angle. For most cases involving microwave radiation, relation (5) applies. Relation (6) sometimes applies to ice clouds and high microwave frequencies. For pure Rayleigh scattering, relation (5) applies.

The study also found that for finite (three-dimensional) clouds, the sign and magnitude of the polarization can change with cloud size. In addition, it was found that the upwelling polarization signature $T_{B,Q}$ due to spherical particles is typically only a couple of degrees Kelvin and never exceeds 10 K for microwave frequencies. Observed polarization signatures for precipitating clouds are sometimes larger, likely because of oriented nonspherical hydrometeors. Finally, it was found that the differences between using scalar and vector radiative transfer theory are negligibly small when considering spherical particles.

F. CZEKALA

1. Czekala and Simmer (1998)

Unlike the other studies reviewed in this section, Czekala and Simmer (1998) consider only nonspherical liquid water drops and do not examine the effects of nonspherical ice. This is important for understanding how nonspherical water drops can affect microwave radiation. The full Stokes vector formulation of the radiative transfer equation was used to model both upwelling and downwelling microwave radiation from rain modeled as rotationally symmetric ellipsoids with a size-dependent axis ratio. The particles were assumed to be oriented with their rotational axis aligned along the vertical, and azimuthal symmetry was assumed. The model computations were performed at frequencies of 10.7, 19.4, and 37 GHz, and a Marshall–Palmer drop size distribution (Section III.D) was used.

Figure 4 shows results of the difference (nonspherical minus spherical) of $T_{B,Q}$ computations for eight upward viewing angles between 0° and 90° as a function of rainfall rate. The surface emissivity is set to 1, so all polarization differences are due to scattering by the particles. The figure shows that for viewing angles from 8.3° to 51.8°, the difference in the values of $T_{B,Q}$ between the nonspherical and the spherical particles increases with frequency and rain rate. At larger viewing angles, the difference between the two types of particles is frequency dependent: At high frequencies the brightness temperatures begin to saturate so the differences do not increase, but the differences at the lower frequencies continue to increase.

The authors noted that for the various cases examined, the total intensity (or, equivalently, the average of the horizontal and vertical brightness temperature) for both the upwelling and the downwelling cases did not differ significantly between the spherical and the nonspherical cases. In all upwelling cases, the nonspherical drops yield larger polarization signals than the spherical drops. For downwelling cases, the polarization difference between spherical and nonspherical drops is negative; that is, the spherical particles produce a larger downwelling polarization signature than the nonspherical particles.

2. Czekala (1998)

This study models oblate and prolate spheroidal ice particles with axial ratios of 5 and 0.2, respectively, and whose axis of symmetry is aligned along the vertical. The ice is positioned between 9 and 10 km height, using an exponential size distribution with a maximum equivalent sphere radius of 200 μm and a fixed ice water content of 0.05 kg/m^2. Results are computed for a frequency of 200 GHz and upwelling viewing angles, with the emphasis placed on near limb-viewing angles.

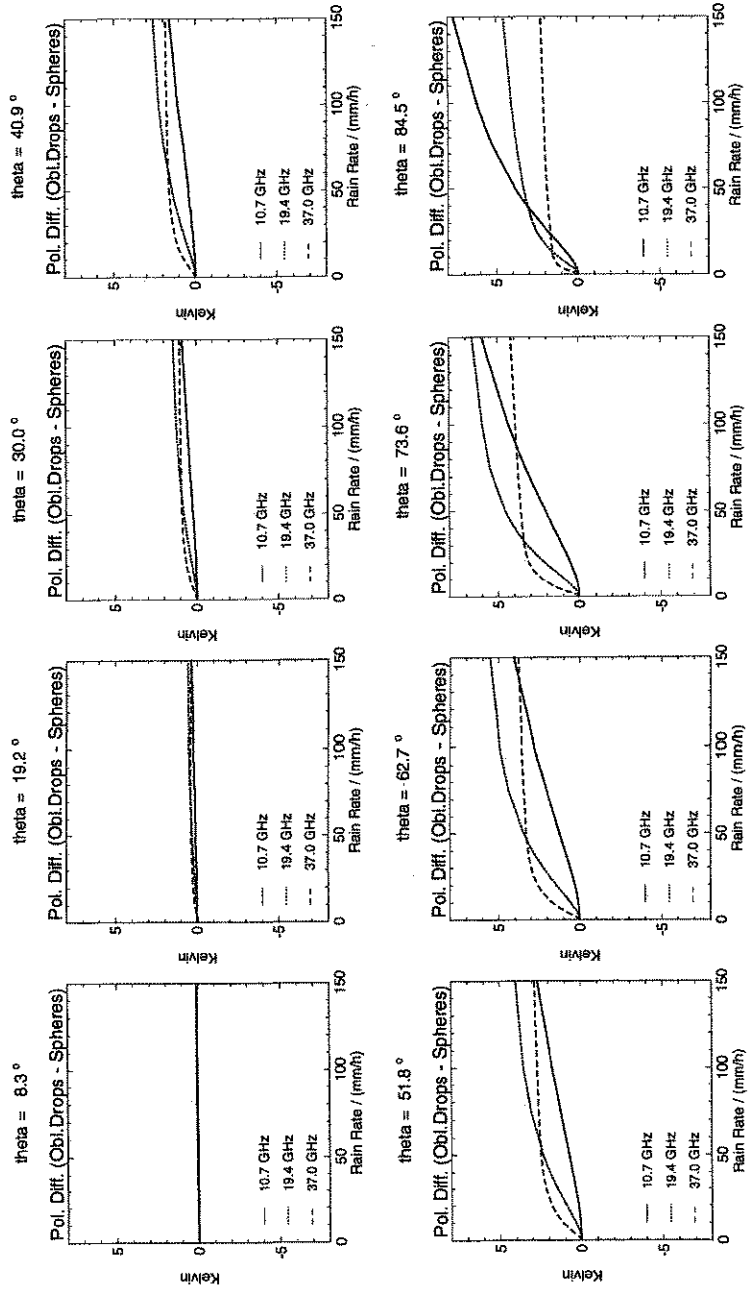

Figure 4 Results of the difference (nonspherical minus spherical) of polarization difference $T_{B,Q}$ computations for eight upward viewing angles between 0° and 90° as a function of rainfall rate. Oriented oblate and spherical liquid rain drops are considered. The surface emissivity is set to 1, so all polarization differences are due to scattering by the particles. Reprinted from H. Czekala and C. Simmer (1998), Microwave radiative transfer with nonspherical precipitating hydrometeors, *J. Quant. Spectrosc. Radiat. Transfer* **60**, 365–374.

The results show that the polarization difference $T_{B,Q}$ for oblate particles is positive for upward directions and negative for downward directions. For prolate particles, the sign of $T_{B,Q}$ is reversed for these situations. The largest magnitude of $T_{B,Q}$ is realized as the viewing angle approaches 90°; for example, $T_{B,Q}$ exceeds 20 K for viewing angles greater than 85°. The differences between spherical and nonspherical particle results for the total intensity $T_{B,I}$ are as large as 10 K for prolate and oblate particles, depending on the viewing direction.

G. Hornbostel

1. Hornbostel *et al.* (1995)

Hornbostel *et al.* (1995) performed radiative transfer computations for downwelling microwave radiation through polydispersions of oriented oblate raindrops and compared the model results with ground-based polarimeter observations. In addition, ground-based measurements of rain rate, disdrometer (drop size) data, and other meteorological quantities were available for comparison with the polarimeter and model data. The results show the potential of inferring drop size distribution parameters by inverting dual-polarized brightness temperatures. In addition, the authors pointed out that measurements of downwelling brightness temperatures from a hydrometeor layer often give larger polarization signatures than those obtained by physical modeling with spherical particles. However, they show that, by modeling raindrops as oblate spheroids, good agreement with measurements is obtained.

2. Hornbostel and Schroth (1995)

This paper uses the method of successive orders of scattering to model the downwelling 20-GHz brightness temperature received by a ground-based radiometer. The model results show that the polarization difference (vertical minus horizontal) is directly related to the drop size distribution (oblate raindrops with their axis of symmetry aligned to the vertical are used). The authors demonstrate that drop size distributions can be derived from measured radiometric polarization differences, and then show how these drop size distributions can be used as input parameters to compute the propagation properties of Earth–satellite communication paths.

3. Hornbostel *et al.* (1997)

This short paper investigates the potential of using the polarization information from a ground-based radiometer to infer information about rainfall drop size distribution parameters. The vector radiative transfer equation is solved for frequencies of 13, 19, 37, and 90 GHz and rain rates ranging from 0 to 100 mm/h. The dependence of downwelling brightness temperatures (and brightness temperature differences) is shown as a function of rain rate for several drop size distributions.

4. Kutuza *et al.* (1998)

The paper by Kutuza *et al.* (1998) shows the possibility for a nonzero third Stokes parameter brightness temperature ($T_{B,U}$) due to scattering by hydrometeors. An important theoretical result of this paper is that for a homogeneous layer of nonspherical oriented raindrops, $T_{B,U}$ is dominated by the first azimuthal harmonic of the emission vector. For downwelling radiation, the model results give values of downwelling $T_{B,U}$ on the order of 2–3 K, depending on the rain rate, frequency, and mean drop canting angle. For a given frequency, downwelling $T_{B,U}$ increases with rain rate, reaches a saturation value, and then decreases. For a given rain rate, downwelling $T_{B,U}$ increases with frequency. Upwelling $T_{B,U}$ over an ice crystal layer reach values of about 4–5 K.

5. Schroth *et al.* (1998)

The paper by Schroth *et al.* (1998) is a follow-up study to the Kutuza *et al.* (1998) paper and shows the importance of including solar effects on modeling of downwelling $T_{B,U}$. For example, it is shown theoretically that, for microwave frequencies and realistic nonspherical raindrop canting angles, the resulting $T_{B,U}$ is about 2 or 3 K. However, including incident solar radiation increases these values by 5–7 times.

H. Other Work

1. Smith and Mugnai (1989)

The paper by Smith and Mugnai (1989) is the third in a series of papers that investigates the effect of hydrometeors on upwelling microwave brightness temperatures. The study only considers spherical particles, but it is worthy of mention here because the series of papers was seminal in its use of a time-dependent three-dimensional cloud microphysics model as input to a plane-parallel radiative transfer model. From a physical perspective, the modeling effort in these studies was quite extensive and included several types of hydrometeors (rain, cloud, graupel, hail, ice crystals). In addition, the radiative effects of ice size, ice density, and mixed-phase layers were examined. The studies of scattering by nonspherical

hydrometeors mentioned in the preceding sections have all used ad hoc atmospheric models; thus, it would be important to extend the microphysical cloud model approach of Smith and Mugnai (1989) to include nonspherical particles to gain a better understanding of the importance of nonsphericity on microwave scattering by precipitation. Roberti and Kummerow (1999) have recently made some progress on this challenge.

2. O'Brien and Goedecke (1988a, b)

These papers considered polarized microwave scattering by dendritic snow crystals at a 10-mm wavelength (30-GHz frequency). The studies examined the effect of complex refractive index mixing rules, equivalent particle shape and size, and mono- versus poly-disperse distributions on radiative cross sections and forward scattering matrix elements. Solutions of the radiative transfer equation were not performed, but the studies are fundamental in understanding the microwave scattering properties of snow.

3. Tsang

The textbook by Tsang *et al.* (1985) provides an extremely comprehensive and detailed coverage of the theory of microwave remote sensing, including treatments of the vector radiative transfer equation and scattering by nonspherical particles. The textbook includes several examples of scattering by precipitation. The paper by Tsang (1991) lays the theoretical foundation for exploring the potential of using passive microwave polarimetry (i.e., using all four components of the Stokes vector) on remote sensing of geophysical terrain. Though the paper is geared toward remote sensing of forests and vegetation, the formulation is completely general.

4. Three-Dimensional Studies

As mentioned previously in Section E, Liu *et al.* (1996b) and Liu and Simmer (1996) were the first to publish results of a three-dimensional polarized microwave radiative transfer model to compute upwelling brightness temperatures for precipitating atmospheres. Their results pertained to spherical particles only. Their Monte Carlo model is capable of treating randomly oriented axisymmetric particles, but cannot handle oriented particles. Haferman *et al.* (1997) presented a three-dimensional polarized radiative transfer model based on the discrete ordinates method and validated the results for plane-parallel atmospheres containing randomly oriented axisymmetric particles. In principle, the model can handle oriented particles, though it so far has not been applied to this type of situation.

Roberti and Kummerow (1999) have developed a three-dimensional "forward–backward" Monte Carlo code that treats spherical and/or randomly oriented nonspherical hydrometeors. They have also developed a forward Monte Carlo code that treats oriented nonspherical hydrometeors, but this code is for plane-parallel situations. However, the code should be extendable to three dimensions. These authors have intercompared some of their three-dimensional polarized computations with favorable results, but this continues to be an active area of research.

5. Other Related Studies

There are many other studies that have considered the propagation of microwave radiation through nonspherical particles. However, most of the studies considering passive remote sensing of precipitation have been reviewed in the preceding pages. Exceptions are the works by Huang and Liou (1983) and Bauer and Schluessel (1993). Both of these studies used the full vector form of the radiative transfer equation for plane-parallel atmospheres, but only considered spherical particles.

Other related studies that do not specifically deal with passive microwave remote sensing of precipitation include the following: several that considered the effect of precipitation on communication transmissions, for example, Oguchi (1960, 1981), Mishchenko (1992a), and Li *et al.* (1995); Macke and Großklaus (1998), who considered the effects of nonspherical particles on lidar remote sensing of precipitation; Jin (1998), who reviewed polarimetric scattering from nonspherical particles as applied to remote sensing of land surfaces; and, finally, Aydin (Chapter 16), who reviewed scattering by hydrometeors in the context of active remote sensing of precipitation.

III. MATHEMATICAL FORMULATION

A. Radiative Transfer Theory

The vector radiative transfer equation (VRTE) for polarized monochromatic radiation is given by Eq. (86) of Chapter 1. For media with thermal emission, for example, atmospheric hydrometeors in the microwave regime, the VRTE includes an additional emission term and is written for plane-parallel geometries as

$$\begin{aligned}\cos\vartheta\frac{d}{dz}\mathbf{I}(z;\vartheta,\varphi) &= -n_0\{\mathbf{K}(z;\vartheta,\varphi)\}\mathbf{I}(z;\vartheta,\varphi)+\mathbf{K}_a(z;\vartheta,\varphi)I_b(T)\\ &\quad+n_0\int_0^{2\pi}\int_{-1}^{1}\{\mathbf{Z}(z;\vartheta,\varphi;\vartheta',\varphi')\}\mathbf{I}(z;\vartheta',\varphi')\\ &\quad\times d(\cos\vartheta')\,d\varphi', \qquad (8)\end{aligned}$$

where the vector $\mathbf{K}_a$ is a four-component absorption coefficient vector with components given by Eqs. (89)–(92) of Chapter 1 and $I_b(T)$ is the Planck blackbody radiance of particles at temperature T. The other terms are defined in Chapter 1, as is the laboratory reference frame in which the z axis and angles ϑ and φ are defined.

The VRTE given by Eq. (8) is completely general for the case of a plane-parallel medium and is the most rigorous and appropriate form of the radiative transfer equation to use for sparsely distributed, preferentially oriented, nonspherical particles. A simpler form of the VRTE is applicable to the situation of an azimuthally symmetric radiation field (note that solar radiation or rough surfaces may entail asymmetry). An example of this situation is a plane-parallel medium containing axisymmetric nonspherical particles aligned parallel to the horizontal (x–y) plane of the laboratory frame (Section III of Chapter 1) and randomly aligned in azimuthal directions, with thermal emission as the only source of radiation. For such a situation, the third and fourth Stokes parameters are identically equal to zero, and the VRTE reduces to

$$\cos\vartheta \frac{d}{dz}\mathbf{I}(z;\vartheta) = -n_0\{\mathbf{K}(z;\vartheta)\}\mathbf{I}(z;\vartheta) + \mathbf{K}_a(z;\vartheta)I_b(T) + n_0\int_{-1}^{1}\{\mathbf{Z}(z;\vartheta,\vartheta')\}\mathbf{I}(z;\vartheta')\,d(\cos\vartheta'), \tag{9}$$

where the Stokes vector is now $\mathbf{I} = [I, Q]^T$ (T means transpose) and all vectors and matrices are of length 2 and dimension 2×2, respectively [however, the (2, 2) element of the phase matrix is computed using the (3, 3) element of the scattering matrix; see Eq. (68) of Chapter 1]. Finally, for the case of randomly oriented axisymmetric particles in a plane-parallel, azimuthally symmetric radiation field, the extinction matrix and absorption coefficient vector become scalars and the VRTE reduces to

$$\cos\vartheta \frac{d}{dz}\mathbf{I}(z;\vartheta) = -n_0 C_{ext}\mathbf{I}(z;\vartheta) + n_0 C_{abs} I_b(T) + n_0\int_{-1}^{1}\{\mathbf{Z}(z;\vartheta,\vartheta')\}\mathbf{I}(z;\vartheta')\,d(\cos\vartheta'), \tag{10}$$

where the extinction and absorption cross sections C_{ext} and C_{abs} are defined in Section XI of Chapter 1, $\mathbf{I} = [I, Q]^T$, and $\mathbf{Z}$ has dimension 2×2 [see the note regarding the scattering matrix following Eq. (9)]. For unpolarized radiation, Eq. (10) reduces to the more familiar scalar radiative transfer equation.

Several methods for numerically solving the VRTE are described in the literature. Most of these methods use discrete angles and quadrature summation to simplify the integration term that appears in Eqs. (8)–(10). An exception is the Monte Carlo method, which uses probabilistic interaction laws to trace photons through a medium. Overviews of Monte Carlo methods for solving the VRTE are given by Adams and Kattawar (1993) and Marchuk *et al.* (1980). Descriptions of backward (or adjoint) Monte Carlo methods, which trace photons from a detector back to a source, are given by Liu *et al.* (1996b) and Roberti and Kummerow (1999).

Other numerical techniques for solving the plane-parallel VRTE include the method of successive orders of scattering (Hornbostel and Schroth, 1995; Liu and Simmer, 1996; Czekala and Simmer, 1998), the matrix operator method (Liu *et al.*, 1991), the method of invariant embedding (Adams and Kattawar, 1970), the Gauss–Seidel method (Herman *et al.*, 1995), the matrix-eigenvalue technique (Ishimaru, 1978), the iterative method (Tsang *et al.*, 1984; Jin, 1991; Kuga, 1991), the adding method (Hansen, 1971; Hovenier, 1971; Evans and Stephens, 1991), and the discrete ordinates method (Haferman *et al.*, 1997; Schulz *et al.*, 1999b). This list is not intended to be exhaustive, but is provided to give the reader an entry to the terminology and literature.

It should be noted that some VRTE solution methods with differing names are quite similar to one another, whereas some methods with the same names but different authors can be very different from one another. For example, the adding method of van de Hulst (1980) is a special case of the matrix operator method (Plass *et al.*, 1973). On the other hand, Evans and Stephens (1991) note that their adding method is very different from that described by Hansen (1971).

B. Radiative (Single-Scattering) Properties

The radiative properties for the VRTE in general depend on direction; position; wavelength; and particle size, composition, and orientation. For a small volume of independent scatterers, the radiative properties of the volume are computed by averaging the single-scattering properties of the volume of scatterers over size, shape, and orientation (Section X of Chapter 1). To define the scattering volume for single-scattering purposes, it suffices to specify:

a. The particle size distribution $N(r)\,dr$ that gives the number of particles per unit volume having an equivalent-sphere radius between r and $r + dr$ and satisfies the normalization $\int_{r_{min}}^{r_{max}} N(r)\,dr = n_0$ (where r_{min} and r_{max} are the minimum and maximum radii of the distribution)
b. A definition of an equivalent sphere (e.g., an equivalent sphere may be defined as a sphere having an equal volume or an equal average projected cross-sectional area to a given nonspherical particle)
c. A description of the particle shape, for example, the particle aspect ratio a/b, where $a/b < 1$ for prolate spheroids and $a/b > 1$ for oblate spheroids, with a and b representing the lengths of the nonrotational and symmetry axes, respectively

d. The refractive index of the particle
e. The wavelength under consideration

Given these specifications, the solution to Maxwell's equations for the scattered field of the polydispersion of particles in terms of the ensemble-averaged phase matrix (Chapter 1, Section VI) may be computed. The scattering properties needed for the VRTE may then be computed according to the formulas of Chapter 1.

C. Size Distribution

In Chapter 1, the particle size distribution was written as a function of particle radius. For convenience, the particle size distribution is written in the remainder of this chapter as a function of particle diameter (for notes on converting size distributions between diameter and radius, see Appendix A). Using this convention, the particle size distribution $N(D)$ gives the number of particles per unit volume with diameters between D and $D + dD$. In the case of nonspherical particles, the distribution gives the number of particles per unit volume with *equivalent-sphere* (Appendix B) diameters between D and $D + dD$. The most general size distribution commonly employed in microwave precipitation studies is the modified gamma distribution for spherical particles, written as

$$N(D) = N_0(\Lambda D)^{P_1} \exp\left[-(\Lambda D)^{P_2}\right], \tag{11}$$

where N_0, Λ, P_1, and P_2 are parameters. Gasiewski (1993) provides expressions for computing quantities such as mean diameter, diameter variance, mode diameter, total particle number density, fractional volume, liquid and ice water density, and reflectivity, using this distribution. Setting $P_1 = 0$ and $P_2 = 1$ reduces Eq. (11) to an exponential distribution

$$N(D) = N_0 \exp[-(\Lambda D)]. \tag{12}$$

Of particular significance is the Marshall–Palmer distribution, which results by setting

$$\left.\begin{aligned} N_0 &= 8000\,\mathrm{m}^{-3}\,\mathrm{mm}^{-1} \\ \Lambda &= 4.1R^{-0.21}\,\mathrm{mm}^{-1} \end{aligned}\right\} \text{Marshall–Palmer,} \tag{13}$$

where R is the rain rate in millimeters per hour. The Marshall–Palmer distribution is very widely used in precipitation modeling to describe the size distribution of liquid raindrops. The drop size distribution can vary greatly over meteorological conditions, but the Marshall–Palmer distribution is a good representation of "average" rainfall. Bauer *et al.* (1998) have used the exponential distribution of

Table I

Sample Coefficients of Exponential Size Distribution for Four Hydrometeor Types [i.e., Eq. (12): $N(D) = N_0 \exp(-\Lambda D)$; $N_0 = c_1 R^{c_2}$; $\Lambda = c_3 R^{c_4}$; R Is the Rain Rate in mm/h]. $D_{\min}$ and $D_{\max}$ Are the Minimum and Maximum Diameters in the Size Distribution, and ρ Is the Particle Density

Hydrometeor type	c_1 ($\mathrm{m}^{-3}\,\mathrm{mm}^{-2}\,\mathrm{h}$)	c_2	c_3 ($\mathrm{mm}^{-3}\,\mathrm{h}$)	c_4	$D_{\min}$ (mm)	$D_{\max}$ (mm)	ρ ($\mathrm{g\,m}^{-3}$)
Rain	7000	0.37	3.8	−0.14	0.2	2.5	1
Snow	1500	−0.38	2	−0.34	0.5	5	0.2
Graupel	3400	−0.01	2.2	−0.24	0.5	3	0.5
Hail	12.1	0	0.42	0	1	35	0.9

Source: Based on Bauer *et al.* (1998).

Eq. (12) to model four hydrometeor particles (rain, snow, graupel, and hail). Details are provided in Table I.

Another distribution that is commonly employed is the gamma distribution

$$N(D) = N_0 D^P \exp[-\Lambda D], \tag{14}$$

which has the three parameters N_0, Λ, and P. Evans and Stephens (1995a) have used this distribution to model nonspherical ice crystals and suggest that the integration over a discrete size distribution [cf. Eq. (50) of Chapter 1] be performed using

$$\int_0^\infty N(D)k(D)\,dD \approx \sum_{i=1}^{N} k(D_i) \int_{D_i^{\mathrm{l}}}^{D_i^{\mathrm{u}}} N(D)\left(\frac{D}{D_i}\right)^{\zeta} dD = \sum_{i=1}^{N} n_i k(D_i), \tag{15}$$

where $k(D_i)$ represents a scattering property of a single particle in the ith bin, D_i^{l} and D_i^{u} are the lower and upper bounds of the ith bin, and the weight $(D/D_i)^{\zeta}$ is introduced to account for increasing contribution to the scattering properties with increasing size. For the gamma distribution, it follows that n_i may be written as

$$n_i = N_0 D_i^{-\zeta} \Lambda^{-(P+\zeta+1)}\left[\Gamma\left(P+\zeta+1, \Lambda D_i^{\mathrm{u}}\right) - \Gamma\left(P+\zeta+1, \Lambda D_i^{\mathrm{l}}\right)\right], \tag{16}$$

where $\Gamma(a, x)$ is the incomplete gamma function. A value of $P = 0$ yields an exponential distribution, though values of $P = 1$ and $P = 2$ are also typically used (as P increases, the width of the distribution decreases). Schneider and Stephens (1995) suggest a range of 0 to 6 for the parameter ζ.

D. Shape Distribution

1. Raindrops

Pruppacher and Pitter (1971) parameterized the shape of the surface of a raindrop using a series of Chebyshev polynomials that defines the radius of the raindrop with respect to the polar angle θ via

$$r(\theta) = r_0\left(1 + \sum_{n=0}^{\infty} c_n \cos(n\theta)\right), \tag{17}$$

where r_0 is the radius of the undistorted spherical drop. This equation generates shapes that are consistent with observations showing that falling raindrops typically have a nearly oblate shape with a nearly round top and flattened bottom, where the flat bottom tends to become more extreme as the particle increases in size. For spheroids, shape can be characterized by defining the particle aspect ratio a/b, where a and b are the lengths of the nonrotational and symmetry axes (sometimes in the literature, a and b refer instead to the particle semi-major and semi-minor axes, or vice versa). The spheroid is "oblate" when $a/b > 1$, "prolate" when $a/b < 1$, and spherical for $a/b = 1$. In some of the equations that follow, the ratio b/a will be used to uphold the conventions defined in this paragraph.

A recently published set of coefficients for Eq. (17) is presented by Chuang and Beard (1990), who parameterize the aspect ratio b/a as a function of equivalent spherical raindrop diameter D (in centimeters) using (the coefficient of the second term has been corrected according to personal communication with K. Beard)

$$\frac{b}{a} = 1.01668 - 0.098055D - 2.52686D^2 + 3.75061D^3 - 1.68692D^4. \tag{18}$$

This equation is useful for approximating raindrops as oblate particles and is valid for the diameter range 0.1–0.9 cm. Other parameterizations of the particle aspect ratio for raindrops have been reviewed by Chandrasekar *et al.* (1988). The most recent work by Beard and co-workers (Andsager *et al.*, 1999) gives the following formula for nonoscillating drops (e.g., raindrops in the presence of an electric field) (D in centimeters):

$$\frac{b}{a} = 1.0048 + 0.0057D - 2.628D^2 + 3.682D^3 - 1.677D^4, \tag{19}$$

valid for the diameter range 0.1–0.9 cm, and, for oscillating raindrops,

$$\frac{b}{a} = 1.012 - 0.1445D - 1.028D^2, \tag{20}$$

valid for the diameter range 0.1–0.44 cm. The preceding formula is from a fit to measurements from several published results.

2. Ice

Ice crystals (e.g., plates, dendrites, and columns), which tend to assume a preferential orientation, take on a wide variety of shapes. Matrosov *et al.* (1996) have compiled a list of coefficients to describe ice crystal shapes for use in the formulas

$$d = a_2 L^f, \tag{21}$$

$$\rho = a_1 L^c, \tag{22}$$

where d (cm) is the crystal thickness, L (cm) is the maximum particle dimension, and ρ is the ice crystal density (g cm^{-3}). The coefficients a_1, a_2, f, and c are listed in Table II. Wang (1997) has used elementary mathematical functions to

Table II

Coefficients of the Bulk Density—Size and Thickness—Major Dimension Relationships [i.e., Eq. (21) Thickness: $d = a_2 L^f$; Eq. (22) Density: $\rho = a_1 L^c$] for Different Ice Crystal Classes. Except for Aggregates, Dimensions Are in Centimeters and Densities Are in Grams per Cubic Centimeter. For Aggregates, $\rho(\text{g cm}^{-3}) = 0.07S^{-1.1}$, where S Is the Particle Major Dimension in mm, and the Particle Shape Can Be Modeled as Prolate and Oblate Spheroids

Ice crystal class	a_1	a_2	f	c
Dendrites	0.25	0.009	0.377	−0.377
Solid thick plates	0.916	0.138	0.778	0.0
Hexagonal plates	0.916	0.014	0.474	0.0
Solid columns ($L/d \leq 2$)	0.916	0.578	0.958	0.0
Solid columns ($L/d > 2$)	0.916	0.260	0.927	0.0
Hollow columns ($L/d \leq 2$)	0.53	0.422	0.892	−0.092 (cold)
	0.82			−0.014 (warm)
Hollow columns ($L/d > 2$)	0.53	0.263	0.930	−0.377 (cold)
	0.82			−0.014 (warm)
Long solid columns	0.916	0.035	0.437	0.0
Solid bullets ($L \leq 0.03$ cm)	0.916	0.153	0.786	0.0
Hollow bullets ($L > 0.03$ cm)	0.77	0.063	0.532	−0.0038
Elementary needles ($L < 0.05$ cm)	0.916	0.030	0.611	0.0
Aggregates (see table caption)				

Source: Based on Matrosov *et al.* (1996).

represent the size and shape of ice crystals. The relationship between a given ice crystal and the diameter of a sphere of equivalent volume is discussed by Evans and Stephens (1995a).

Hail and graupel are ice hydrometeors that are in general larger than the ice crystals mentioned previously. Hail and graupel are usually spheroidal or conical in shape and tend to tumble or wobble when falling and do not generally assume a preferential orientation. Wang (1982) has proposed a very general function to describe the shape of hail and graupel and has also provided expressions for cross-sectional area, volume, and surface area of the particle. Turk and Vivekanandan (1995) modeled the shape of graupel as a cone with a 45° half angle connected to a half-oblate spheroidal bottom, which is related to an equal volume sphere according to

$$D^3 = \frac{b^2}{2}h + a. \tag{23}$$

In Eq. (23), a and b are the semi-minor and semi-major axes of the spheroidal bottom, h is the cone height, and D is the diameter of the equal volume sphere. Matson and Huggins (1980) studied hailstones falling in their natural environment and found that 84% of the observed hailstones were spherical and the remainder were roughly conical. However, in one storm, they found roughly half of the hailstones to be conical. Overall, they found the mean ratio of minimum to maximum hailstone dimensions to be about 0.77. The results of Bringi *et al.* (1986a, b) imply that the relations for rain given by Eqs. (18)–(20) are reasonable approximations for hail and graupel.

For mixed-phase particles (e.g., melting particles), Schols *et al.* (1997) used the linear relationship

$$\frac{a}{b} = f\left(\frac{a}{b}\right)_{\text{liquid}} + (1-f)\left(\frac{a}{b}\right)_{\text{ice}}, \tag{24}$$

where f is the fraction of the particle that is melted and $(a/b)_{\text{liquid}}$ and $(a/b)_{\text{ice}}$ are the aspect ratios for liquid and ice phase particles, respectively, for a given equivalent spherical diameter.

E. Orientation Distribution

The orientation distribution (see Section X of Chapter 1) used in the majority of studies of nonspherical hydrometeor scattering for passive microwave precipitation retrieval has been such that the particles are either randomly oriented [Eq. (54) of Chapter 1] or perfectly aligned along an axis of symmetry [Eq. (55) of Chapter 1] (with the exception of the work by Kutuza *et al.*, 1998). As mentioned in Section D, observational evidence indicates that raindrops fall with a flattened bottom (Pruppacher and Pitter, 1971), ice crystals tend to fall with their long axis aligned perpendicular to the direction of fall (but because of electrification sometimes orient themselves with their long axis parallel to the fall direction; see Caylor and Chandrasekar, 1996), and graupel and hail tumble and wobble as they fall (Matson and Huggins, 1980). Examples of nonrandom orientation distributions are the truncated Gaussian distribution used by Aydin and Tang (1997a)

$$p(\beta) = \frac{\exp[-(\beta-\overline{\beta})^2/2\sigma^2]}{\int_0^{\pi/2}\exp[-(\beta-\overline{\beta})^2/2\sigma^2]\sin\beta\,d\beta}, \tag{25}$$

where $\overline{\beta}$ is the mean drop canting angle and σ is the standard deviation, and the harmonic oscillator distribution of Vivekanandan *et al.* (1991)

$$p(\beta) = \frac{1}{\pi\beta_{\text{m}}}\left[1-\left(\frac{\beta-\overline{\beta}}{\beta_{\text{m}}}\right)^2\right]^{-1/2}, \tag{26}$$

where β_{m} is the amplitude. Equation (26) must be normalized to unity over the range $\overline{\beta} \pm \beta_{\text{m}}$. Equations (25) and (26) are one-dimensional probability distributions in β. Other examples of one-dimensional orientation distributions are given by Mishchenko (1991b) and Karam *et al.* (1995). Multidimensional orientation distributions are given by Metcalf (1988), Holt (1984), and Tsang (1991).

F. Complex Refractive Index

The amplitude matrix (defined in Section IV of Chapter 1) requires specification of a particle complex refractive index

$$m \equiv m_{\text{r}} + im_{\text{i}}, \tag{27}$$

where the real part m_{r} is related to how fast light propagates through the species and the imaginary part m_{i} is related to how much radiation the species absorbs. For liquid water, Ray (1972) has used an extension of Debye theory to obtain refractive indices of water ranging from −20 to 50°C and ice from −20 to 0°C. A more recent tabulation of the complex refractive index of ice has been given by Warren (1984). Both the Ray (1972) and the Warren (1984) studies cover a large portion of the electromagnetic spectrum, including the microwave. For the refractive index of ice in the microwave, m_{r} has an approximately constant value of 1.78 for all frequencies and temperatures, whereas m_{i} is weakly frequency and temperature dependent and ranges from about 10^{-4} to 10^{-2} (very weak absorption). The

refractive index for liquid water in the microwave has a stronger frequency and temperature dependency, with m_r ranging from between about 3 and 10 and m_i ranging from approximately 0.5 to 3 (strong absorption) for microwave frequencies and common atmospheric temperatures.

The complex refractive index of mixtures (e.g., porous ice consisting of ice and air, or spongy ice consisting of ice and water) is treated in detail in Chapter 9. Bohren and Battan (1982) also cover this topic and compare the Maxwell-Garnett (treatment of a mixture as a nonsymmetric host and inclusion) versus the Bruggeman (treatment of the substances as symmetric) theories of the effective dielectric constant ($\varepsilon \equiv m^2$) for a two-component mixture. Smith and Mugnai (1989) proffer the following mixing formula for porous ice:

$$m_{\text{mix}} = \left[f_{\text{air}} m_{\text{air}}^2 + (1 - f_{\text{air}}) m_{\text{ice}}^2\right]^{1/2}, \tag{28}$$

where the fraction of air is defined as

$$f_{\text{air}} = 1 - \frac{\rho_p}{\rho_i}, \tag{29}$$

with ρ_p set to the density of porous ice [0.45 gm cm^{-3} in the Smith and Mugnai (1989) study] and ρ_i set to the density of pure ice (0.91 gm cm^{-3}). The refractive index of moist air is given by Battan (1973) as

$$m_{\text{air}} = 1 + 10^{-6}\left[\frac{77.6}{T}\left(P + 4810\frac{e_v}{T}\right)\right], \tag{30}$$

where P is the air pressure and e_v is the partial pressure of water vapor, both in millibars. An alternate relationship for the complex refractive index of an ice–air mixture is given by Matrosov *et al.* (1996) as

$$\frac{m_{\text{mix}}^2 - 1}{m_{\text{mix}}^2 + 2} = (1 - f_{\text{air}})\frac{m_{\text{ice}}^2 - 1}{m_{\text{ice}}^2 + 2}. \tag{31}$$

Finally, a formulation for computing the refractive index of most snow based on Debye theory is given by Sadiku (1985).

G. Hydrometeor Terminal Velocity

Some of the size distributions described in Section C use the rain rate R as a parameter. This value of R should be considered a *nominal* rain rate; the true rain rate (ignoring vertical air velocities) is given by

$$R = \int v(D)N(D)V(D)\,dD, \tag{32}$$

where $v(D)$ is the terminal velocity of a particle with equivalent spherical diameter D and $V(D)$ is the particle volume. Because nonspherical particles could have significantly more or less drag force exerted on them as they fall, the rain rate computed using Eq. (32) could differ for an identical volume of spheres versus nonspheres. Expressions for $v(D)$ for various precipitation particles are given by Mitchell (1996).

H. Modeling the Atmosphere

In general, solution of the VRTE requires specification of a model atmosphere, including profiles of density, pressure, temperature, and atmospheric gases. Ulaby *et al.* (1981) provide formulas for these quantities for the U.S. standard atmosphere. Most researchers prescribe an ad hoc atmosphere for performing simulations, though several studies have used cloud models (e.g., Smith and Mugnai, 1989; Roberti *et al.*, 1994).

In the microwave region of the spectrum, gaseous absorption and emission are due to water vapor and oxygen; no other species contribute significantly in this spectral region. For water vapor, the model by Liebe *et al.* (1993) with the updates suggested by Rosenkranz (1998) is arguably the best microwave water vapor model available. A state-of-the-art model for microwave attenuation by gaseous oxygen is described by Liebe *et al.* (1992).

I. Modeling the Surface

1. Boundary Conditions

The boundary conditions for the VRTE may be written as

$$\mathbf{I}^+(z_0) = \psi I_b(T_0) + (1 - f_d)\mathbf{R}_s\mathbf{I}_m^- + \frac{f_d}{\pi}\left[\mathbf{R}_d\mathbf{I}_c^- + \int_0^{2\pi} v\mathbf{R}_d\mathbf{I}^-\,d\varphi'\right], \tag{33}$$

$$\mathbf{I}^o(z_1) = \mathbf{I}_{ba}^o + \mathbf{I}_c^o\,\delta(\vartheta - \vartheta')\,\delta(\varphi - \varphi'), \tag{34}$$

where the superscripts $+$, $-$, and o represent radiation moving from the lower boundary at $z = z_0$ toward the domain, from the domain toward the lower boundary, and from outside the upper boundary at $z = z_1$ toward the domain, respectively. The vectors $\mathbf{I}_{ba}$ and $\mathbf{I}_c$ denote background and collimated radiation, respectively, $\mathbf{I}_m^-$ is the Stokes vector in the direction mirroring that of $\mathbf{I}^+$, and $\delta(\,)$ is the Dirac delta function. The symbol f_d is set to 1 for the case of dif-

fuse reflection and is set to 0 for the case of specular reflection. The symbol ψ denotes the emission vector, $I_b(T_0)$ is the Planck blackbody radiance for the surface at temperature T_0, and the symbols $\mathbf{R}_s$ and $\mathbf{R}_d$ are the bidirectional reflectance matrices for specular and diffuse reflection, respectively. Finally, ν is the cosine of the angle between the propagation direction and the normal to the boundary under consideration. Equation (33) states that the Stokes vector for radiation leaving the surface at $z = z_0$ is due to emission plus contributions from specularly and diffusely reflected radiation. Equation (34) states that radiation transmitted from outside the boundary at $z = z_1$ is due to background and collimated radiation (collimated radiation is generally ignored for microwave applications).

2. Lambertian (Diffuse) Surfaces

A Lambertian, or diffuse, surface is an idealized surface that is "perfectly" rough and therefore emits and reflects equally in all directions. For such a surface, in which the reflected radiation is unpolarized, the bidirectional reflection matrix is given by

$$\mathbf{R}_d = \begin{pmatrix} \rho_0 & 0 & 0 & 0 \\ 0 & 0 & 0 & 0 \\ 0 & 0 & 0 & 0 \\ 0 & 0 & 0 & 0 \end{pmatrix}, \tag{35}$$

where ρ_0 is the hemispherical reflectance at the boundary. The emission vector for a Lambertian surface is given by

$$\psi = \begin{pmatrix} \psi_0 \\ 0 \\ 0 \\ 0 \end{pmatrix}, \tag{36}$$

where ψ_0 is the unpolarized hemispherical emittance of the boundary. For the case of a diffusely reflecting boundary, the emission vector given by Eq. (36) is used in Eq. (33) with $f_d = 1$.

3. Fresnel (Specular) Surfaces

A Fresnel, or specular, surface is an idealized surface that is "perfectly" smooth. For such a surface, the reflected radiation is polarized and angle dependent, and the bidirectional reflection matrix is given by (Tsang *et al.*, 1985)[4]

$$\mathbf{R}_s = \begin{pmatrix} \frac{1}{2}\left(|R_v|^2 + |R_h|^2\right) & \frac{1}{2}\left(|R_v|^2 - |R_h|^2\right) & 0 & 0 \\ \frac{1}{2}\left(|R_v|^2 - |R_h|^2\right) & \frac{1}{2}\left(|R_v|^2 + |R_h|^2\right) & 0 & 0 \\ 0 & 0 & \mathrm{Re}\left(R_v R_h^*\right) & \mathrm{Im}\left(R_v R_h^*\right) \\ 0 & 0 & -\mathrm{Im}\left(R_v R_h^*\right) & \mathrm{Re}\left(R_v R_h^*\right) \end{pmatrix}, \tag{37}$$

where the vertical and horizontal reflection coefficients are given by the Fresnel relations

$$R_v(\mu) = \frac{m^2\mu - \sqrt{m^2 + \mu^2 - 1}}{m^2\mu + \sqrt{m^2 + \mu^2 - 1}}, \tag{38}$$

$$R_h(\mu) = \frac{\mu - \sqrt{m^2 + \mu^2 - 1}}{\mu + \sqrt{m^2 + \mu^2 - 1}}, \tag{39}$$

where $\mu = \cos\vartheta$. The radiation emitted by a purely specularly reflecting surface is also polarized and angle dependent, and the emission vector is given by

$$\psi = \begin{pmatrix} 1 - \frac{1}{2}\left(|R_v|^2 + |R_h|^2\right) \\ -\frac{1}{2}\left(|R_v|^2 - |R_h|^2\right) \\ 0 \\ 0 \end{pmatrix}. \tag{40}$$

For the case of a specularly reflecting boundary, the emission vector given by Eq. (40) is used in Eq. (33) with $f_d = 0$.

4. Rough Surfaces

The boundary conditions stated in the preceding sections assume that the surface is perfectly rough or smooth. However, realistic surfaces require a more complicated surface emission vector and reflection matrix. Tsang *et al.* (1985, pp. 70, 203) draw upon the classic work of Beckmann and Spizzichino (1963) to develop upper and lower limits for the reflection matrices for random rough surfaces for all four Stokes parameters. More recently, Gasiewski and Kunkee (1994) have developed a tilted-facet geometrical optics model to obtain expressions for the emission vector and reflection matrix for the first three Stokes parameters, and Yueh (1997)

[4]The sign of U differs between Chapter 1 and Tsang *et al.* (1985). Therefore, the sign of the [3, 4] and [4, 3] elements in the reflection matrix given here also differs from Tsang *et al.* (1985).

has presented a two-scale scattering model (Bragg scattering by small-scale waves plus coherent reflection by large-scale waves) to accurately describe the emission and reflection for all four Stokes parameters.

IV. EXAMPLES OF MODEL ATMOSPHERE SIMULATIONS AND RESULTS

In this section, a simple atmospheric model containing nonspherical hydrometeors is described and polarized microwave radiative transfer results are presented. These examples are simple enough so that interested researchers may use the results as benchmarks.

A. Description of Model Atmosphere

The atmospheric system used for the examples in this section is based on the microwave example of Evans and Stephens (1991), but is modified to incorporate spheroidal particles. The system is summarized in Table III. The system consists of two 4-km-thick layers, where the upper layer contains spheroidal ice particles, the lower layer contains spheroidal raindrops, and the temperature profile varies linearly within each layer such that $T = 300$ K at the surface, $T = 273$ K at the ice/rain interface, and $T = 245$ K at $z = 8$ km. The atmospheric gaseous absorption coefficient is set to $k_{\text{gas}} = 0.01$ and $k_{\text{gas}} = 0.15$ km^{-1} for the lower

Table III

Summary of Parameters Used for Model Atmosphere Radiative Transfer Simulations. The Temperature Indicated Is for the Layer Interface; within Each Layer, the Temperature Varies Linearly. The Gaseous Absorption Coefficient k_{gas} Is Constant within Each Layer. T_{back} Is the Equivalent Blackbody Temperature of the Cosmic Background, and m Is the Complex Refractive Index of the Fresnel Surface

$T_{\text{back}} = 2.7$ K			
z (km)	T (K)	$k_{\text{gas},19}$ (km^{-1})	$k_{\text{gas},85}$ (km^{-1})
8	245	0.005	0.01
4	273	0.03	0.15
0	300		
$m = 3.724 + i2.212$			

and upper layers, respectively, at 85 GHz and $k_{\text{gas}} = 0.005$ and $k_{\text{gas}} = 0.03$ km^{-1} for these layers at 19 GHz.

The two-layer atmosphere is placed above a specularly reflecting surface with an index of refraction of $m = 3.724 + i2.212$, representing a smooth ocean surface at a temperature of 300 K. Unpolarized, diffuse, background radiation at a blackbody equivalent temperature of 2.7 K, representative of cosmic background radiation, is incident from above the atmosphere. These boundary conditions are stated as

$$\mathbf{I}^{+}(z = 0\ \text{km}) = \psi I_{\text{b}}(300\ \text{K}) + \mathbf{R}_{\text{s}}\mathbf{I}_{\text{m}}^{-}, \tag{41}$$

$$\mathbf{I}^{\text{o}}(z = 8\ \text{km}) = I_{\text{b}}(2.7\ \text{K}) \times (1, 0, 0, 0)^{\text{T}}, \tag{42}$$

where the various terms are defined following Eqs. (33) and (34) in Section III.I.

B. Single-Scattering Properties of Hydrometeors

For the numerical examples described in the subsequent section, frozen hydrometeors are placed in the upper atmospheric layer and liquid hydrometeors in the lower layer. The radiative properties for a Marshall–Palmer distribution (Section III.C) of randomly oriented axisymmetric particles are computed using the T-matrix method (Chapter 6). The Marshall–Palmer distribution is transformed into a power law distribution so that the integrations required for averaging over size distribution may be done analytically (see Appendix C). The radiative properties for preferentially oriented axisymmetric particles are computed using the DDA (Chapter 5), and the integration over the Marshall–Palmer distribution is performed using Eq. (16). For all of the cases presented, equivalent-volume sphere diameters are used in the Marshall–Palmer distribution to describe the polydispersion. The complex refractive index of ice is computed according to Warren (1984) and of liquid water according to Ray (1972). All frozen hydrometeors are taken as pure ice with a density of 0.91 g cm^{-3}. For all species the lower and upper limits of integration are taken as $r_{\text{min}} = 0.054$ mm and $r_{\text{max}} = 6$ mm, respectively.

The rain rate R in the Marshall–Palmer distribution is hereafter referred to as the *nominal* rain rate, because it is a proxy parameter used to specify the drop size distribution and is not necessarily the *actual* rain rate that would result from Eq. (32). Some results for the radiative properties of randomly oriented liquid water drops at 19 GHz are shown as a function of the *nominal* rain rate R in Fig. 5. Because the particles are randomly oriented and axisymmetric, the radiative properties for the VRTE reduce to scalars. The results in Fig. 5 consider axis ratios of 0.5, 1, and 2 and show that, for a given volume of liquid water, all of the proper-

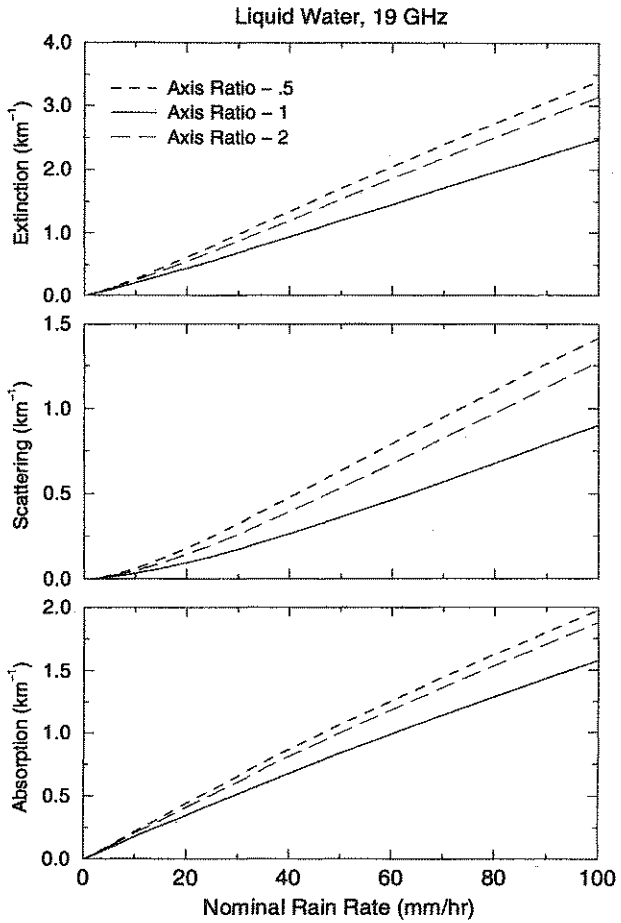

Figure 5 Radiative properties of a Marshall–Palmer distribution of randomly oriented axisymmetric water drops at a frequency of 19 GHz.

ties (extinction, scattering, and absorption coefficient) are largest for the prolate ($a/b = 0.5$) particles, are slightly smaller for the oblate ($a/b = 2$) particles, and are the smallest for the spherical ($a/b = 1$) particles. The trends are the same for liquid water at 85 GHz, though the differences are most extreme for the 19-GHz case.

For ice, the scattering properties of ensembles of randomly oriented axisymmetric particles are not significantly different from those of an equivalent volume of spherical particles (results not shown). On the other hand, the scattering matrix elements (Section XI of Chapter 1) can differ significantly. For example, the scattering matrix components shown in Fig. 6 for spheres versus oblate spheroids with $a/b = 5$ demonstrate that there are large differences at certain scattering angles for elements other than the F_{11} element.

For preferentially oriented nonspherical particles, very large differences in the single-scattering properties can occur for equivalent volumes of different particle shapes. For additional details, the reader should refer to Evans and Stephens (1995a).

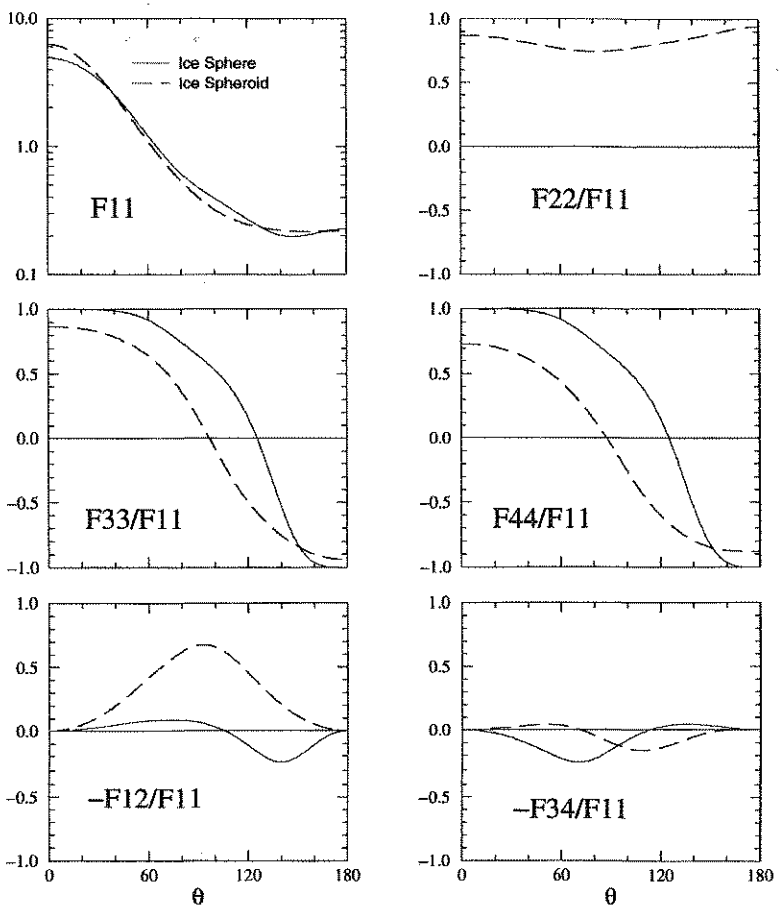

Figure 6 Scattering matrix elements for a Marshall–Palmer distribution of randomly oriented axisymmetric ice particles at a frequency of 85 GHz.

C. Radiative Transfer Results and Discussion

For the results that follow, a Marshall–Palmer distribution of hydrometeors (using equivalent-volume sphere diameters) is placed into each layer as described, and the adding–doubling method (Evans and Stephens, 1991, 1995b) is used to solve the VRTE. The resulting Stokes parameters are transformed into equivalent blackbody temperatures, and results are presented for an upwelling viewing direction of 53° and frequencies of 19 and 85 GHz.

1. Randomly Oriented Axisymmetric Particles

The first example considers randomly oriented axisymmetric ice and liquid hydrometeors. A Marshall–Palmer distribution of ice described by the *nominal* rain rate R is placed into the upper layer, and the same distribution of liquid hydrometeors is placed into the lower layer. The shapes considered are prolate ($a/b = 0.5$), spherical ($a/b = 1$), and oblate ($a/b = 2$), with all particles within the distribution assuming the same shape (i.e., no distribution of shapes is considered). According to the formulas presented in Section III.D, raindrop axial ratios are typically between 0.5 and 1, so giving the entire distribution an axial ratio of 0.5 can be considered an extreme case. Ice particles can take on larger aspect ratios, so for this example, ice axial ratios of $a/b = 0.25$ and 4 are also considered.

In addition to the "base case" that considers rain and ice, cases with rain only and ice only are also considered. Several quantities are defined here for discussion purposes:

$$T_{\mathrm{v},\Delta} = T_{\mathrm{v,sphere}} - T_{\mathrm{v,spheroid}}, \tag{43}$$

$$T_{\mathrm{h},\Delta} = T_{\mathrm{h,sphere}} - T_{\mathrm{h,spheroid}}, \tag{44}$$

$$T_{Q,\Delta} = T_{Q,\mathrm{sphere}} - T_{Q,\mathrm{spheroid}}, \tag{45}$$

where the subscripts v, h, and Q indicate brightness temperatures for vertical, horizontal, and vertical minus horizontal polarizations, and the subscripts "sphere" and "spheroid" indicate the particle shape used in the model atmosphere. In general, at 85 GHz, $|T_{\mathrm{v},\Delta}|$ and $|T_{\mathrm{h},\Delta}|$ are less than 2 K for all cases considered except for the extreme case that considers ice spheroids with axial ratios of 0.25 and 4. In this case, $|T_{\mathrm{v},\Delta}|$ and $|T_{\mathrm{h},\Delta}|$ range from about 5 to 10 K, but $|T_{Q,\Delta}|$ is always less than 2 K.

The most significant departure from spheres is for 19 GHz considering rain only or rain and ice, where $|T_{\mathrm{v},\Delta}|$ and $|T_{\mathrm{h},\Delta}|$ can reach values in excess of 5 K. Figure 7 shows plots of $T_{19\mathrm{h}}$ and $T_{19\mathrm{v},\Delta}$ as a function of R. The plot of $T_{19\mathrm{h}}$ shows that the brightness temperature increases more rapidly with rain rate for spheroids than for spheres. This is because the radiative characteristics for this case (Fig. 5) are larger for the spheroidal particles and, thus, the emission at a fixed low rain

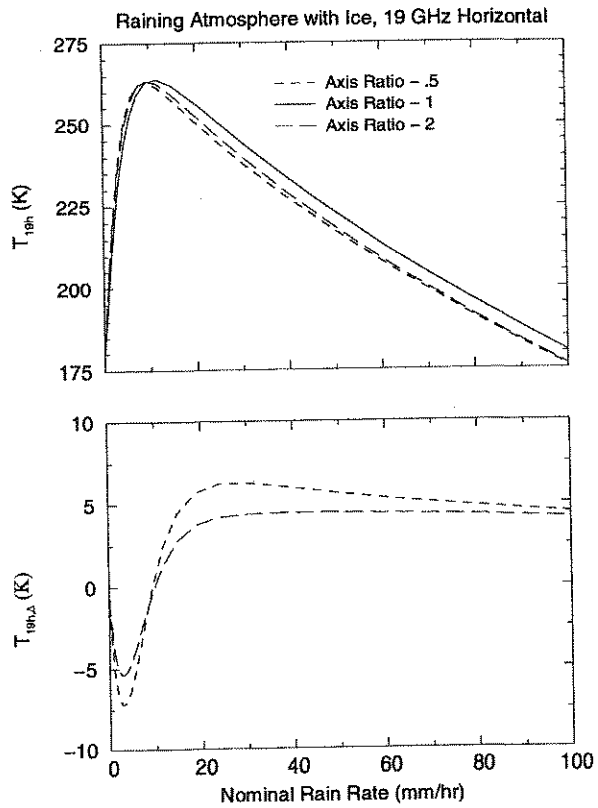

Figure 7 Upwelling 19-GHz brightness temperatures at a viewing angle of 53° for a raining atmosphere with randomly oriented axisymmetric ice and water particles. The atmosphere is described in the text and in Table III. $T_{19\mathrm{h}}$ is the upwelling horizontal brightness temperature, and $T_{19\mathrm{h},\Delta}$ is the difference between spheres and an equivalent volume of spheroids for the 19-GHz horizontally polarized brightness temperature.

rate is stronger for the spheroidal particles ($T_{19\mathrm{h},\Delta} < 0$). At larger rain rates, the opacity and scattering is greater for spheroidal particles, which leads to a larger depression than for spherical particles ($T_{19\mathrm{h},\Delta} > 0$). The results for vertical polarization are similar. Figure 8 shows T_Q for this case, and it also shows the difference $T_{Q,\Delta}$, which exceeds 2 K (to a maximum of nearly 6 K) for rain rates between about 1 and 10 mm/h. Because the raindrop axial ratios considered are extreme, the results should be interpreted as limiting cases.

A final set of cases were run using the previous set of atmospheres as input to the scalar RTE. For randomly oriented axisymmetric particles, the extinction, ab-

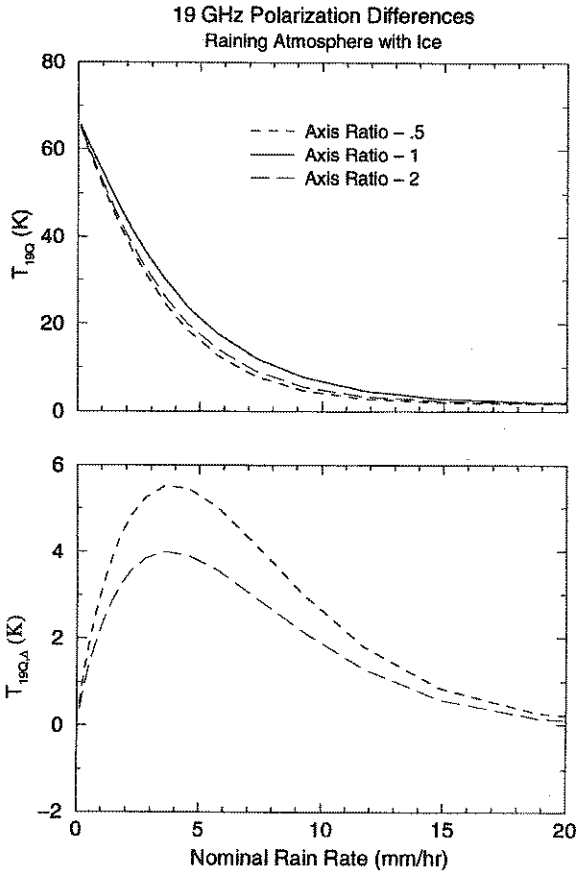

Figure 8 As in Fig. 7, but the polarization difference T_Q ($=T_v - T_h$) is shown. Thus, $T_{19Q,\Delta}$ is the difference of polarization signatures between spheres and an equivalent volume of spheroids for a frequency of 19 GHz.

sorption, and scattering coefficients are scalar quantities. For input to the RTE, the phase function (the [1, 1] element of the scattering matrix) is used, and the vertical or horizontal reflection coefficients (as appropriate) are used at the bottom boundary in order to compute T_v and T_h, respectively. For all of the cases considered, the results from the RTE were always within 2 K of the more rigorous VRTE results as long as the appropriate spheroidal particle properties were used.

It should be noted that this example only considered randomly oriented particles at two frequencies and over a Fresnel surface. It appears that randomly oriented spheroidal particles do not significantly impact radiative transfer results

in comparison to results obtained using spherical particles. However, it would be worthwhile to perform similar numerical experiments using other surface types, additional microwave frequencies, and mixed-phase particles.

2. Preferentially Oriented Axisymmetric Particles

The second example considers ice particles oriented with their long dimension aligned parallel to the ocean surface in the layer from 4 to 8 km. The rain layer from 0 to 4 km is filled with spherical water drops with a constant *nominal* rain rate of $R = 2$ mm/h. Results are compared as a function of ice *nominal* rain rate for spherical ice versus solid ice columns. The aspect ratio for the columns is that from Eq. (21) and Table II, namely, $d = 0.260L^{0.927}$, though the density is fixed at 0.91 gm cm^{-3} for both particle shapes.

Results of the VRTE solution are depicted in Fig. 9. For a given ice *nominal* rain rate, a given percentage of spherical ice is converted to oriented columnar ice for particles with an equivalent spherical diameter of 1 mm or less [see also Evans and Vivekanandan (1990) and Roberti and Kummerow (1999) for similar modeling experiments]. The top panel of Fig. 9 shows how T_{85h} decreases for a fixed rain rate as the fraction of oriented ice columns is increased. The results for T_{85v} (not shown) are largely unaffected by converting spheres to columns. Presumably, this is due to the columns being oriented with their long dimension aligned with the horizontal plane, and thus, the relatively larger scattering and extinction properties along the line of sight (see Evans and Stephens, 1995a) lead to a more depressed horizontally polarized brightness temperature.

Because T_{85h} decreases as the fraction of columns is increased and T_{85v} remains approximately fixed, the polarization difference T_{85Q} (bottom panel of Fig. 9) increases with the fraction of columns. For the case of all spheres, the polarization difference is about 2 K or less for all values of R. However, this value increases by converting spheres to columns and reaches a value of nearly 25 K for a rain rate of about 1.7 mm/h with 100% of the spheres converted to columns.

V. CONCLUSIONS AND RECOMMENDATIONS

This chapter has considered scattering by nonspherical hydrometeors in the problem of passive microwave remote sensing, with particular emphasis placed on modeling microwave radiation propagating through layers of precipitation. Several studies dealing with this topic were reviewed in Section II. In general, most of the previous work has considered spheroidal ice and water particles oriented along an axis of symmetry. Some of the studies considered the effects of conical shaped hail and a few of the others considered dendritic ice crystals of various

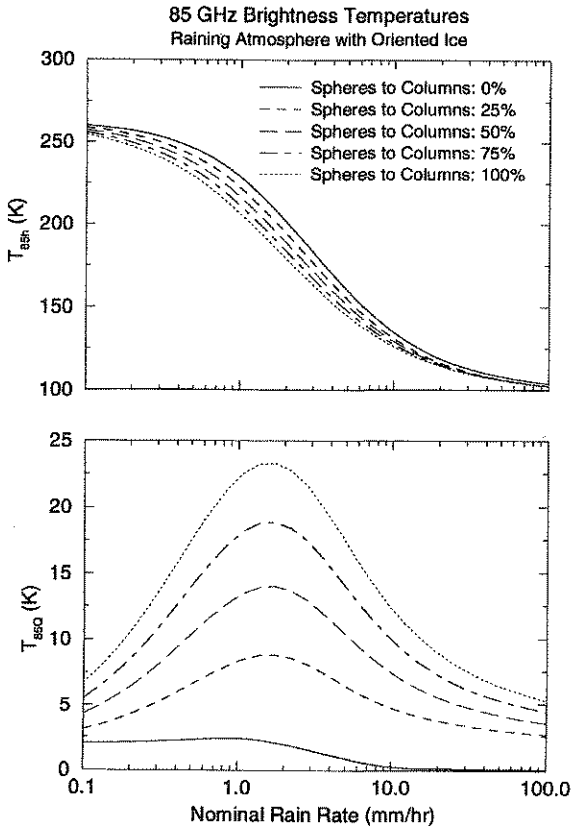

Figure 9 As in Fig. 7, but for oriented ice particles at a frequency of 85 GHz. The lower layer contains spherical water drops at a fixed rain rate of 2 mm/h. The percentage "Spheres to Columns" indicates the percentage of ice spheres at the given *nominal* ice rain rate that are converted to equivalent-volume horizontally oriented ice columns. The upper panel shows the upwelling horizontal brightness temperature T_{85h}, and the lower panel shows the upwelling polarization signature T_{85Q}.

shapes such as columns, plates, and needles. All of the studies found that, theoretically, the oriented nonspherical particles give rise to brightness temperatures that can differ considerably from models that use spherical hydrometeors only. However, the magnitude and sign of the difference between spherical and nonspherical model results depends heavily on frequency, viewing angle, and properties of the underlying surface. A seemingly important practical finding of these studies is that oriented ice and water particles can produce larger polarization signatures (the difference between the vertical and horizontal brightness temperature) than

can be obtained from spherical particles. Observations of polarization signatures up to 13 K from the 85-GHz channel of the SSM/I within stratiform precipitation regions have been reported previously and there are accounts of 37-GHz polarization signatures up to 7 K from airborne radiometers observing tornadic storms over land. If these signatures are truly due to hydrometeors, the studies reviewed here indicate that modeling of such signatures requires the use of oriented nonspherical particles.

Section III provided the necessary mathematical framework for interested researchers to develop their own models of microwave radiative transfer through atmospheres containing nonspherical hydrometeors. The topics covered included the vector radiative transfer equation (incorporating thermal emission and multiple scattering); details regarding single-scattering properties; definition of size, shape, and orientation distributions; and information on the complex refractive indices of water and ice, modeling the surface, and modeling the atmosphere. Details on the numerical methods for solving the equation of transfer are not covered, but references are supplied. The computation of the particle radiative properties are covered in some of the other chapters in this book.

Finally, Section IV presented two examples of microwave radiative transfer through atmospheres containing nonspherical particles. The first example considered an atmosphere with randomly oriented axisymmetric ice and water. The results for this example indicated that, for 19 and 85 GHz over an ocean surface, nonsphericity has a small impact on the radiative transfer results and that there is not much difference between using the scalar and vector radiative transfer theory as long as the appropriate radiative properties are used. The second example considered an atmosphere containing horizontally oriented ice columns and spherical ice over a raining layer. The results for this example showed that the upwelling horizontally polarized 85-GHz brightness temperatures are up to nearly 20 K lower for a case with mixed spheres and columns versus a case with spheres alone. In addition, residual polarization signatures of 5–20 K were found. The results from this second example indicate that polarization signatures that are sometimes observed in precipitation events are very likely due to oriented hydrometeors. Furthermore, to correctly model this type of situation, one must use the rigorous vector radiative transfer theory.

Though several researchers have investigated the topic of nonsphericity in microwave radiative transfer in scattering precipitating atmospheres, there are still several important outstanding issues that require investigation. Foremost among these is the question "What impact does nonsphericity actually have on microwave precipitation algorithms?" The answer to this question, however, depends largely on the ability to correctly model nonspherical particles within microwave radiative transfer models.

One of the important modeling issues that still needs to be developed further is the incorporation of nonspherical particles into three-dimensional, time-

dependent, cloud microphysical structures. In addition, it would be interesting to examine cases that include vertically aligned ice particles, which occur in lightning-producing thunderstorms. Another modeling issue worthy of consideration is the determination of whether detailed particle shape is important in microwave radiative transfer modeling [as an example, it might be possible to model dendritic ice columns with an "equivalent" spheroid—Schneider and Stephens (1995) have touched upon this issue for active remote-sensing applications]. Finally, it is extremely important to continue to gather microwave observations and coincident observations from an independent source to confirm model results. In this way, a better interpretation of microwave signals and an improved accuracy of geophysical retrievals will be attained.

VI. APPENDIX A. PARTICLE SIZE DISTRIBUTION: *N(r)* VERSUS *N(D)*

To relate the independent variables r and D of a given distribution of particles, note that the total number of particles described by each distribution must be identical, that is,

$$\int N(r)\,dr = \int N(D)\,d(D), \tag{A1}$$

which implies that $N(r)\,dr = N(D)\,dD$. But, because $dD = 2dr$, we must have

$$N(r) = 2N(D). \tag{A2}$$

As an example, consider the Marshall–Palmer distribution given by $N(D) = N_0 \exp[-(\Lambda D)]$ with $N_0 = 8000\ \mathrm{m^{-3}\ mm^{-1}}$, $\Lambda = 4.1R^{-0.21}\ \mathrm{mm^{-1}}$, and R is the rain rate in millimeters per hour. Application of Eq. (A2) yields $N(r) = N_{0,r} \exp[-(\Lambda_r r)]$ with $N_{0,r} = 1.6\times10^4\ \mathrm{m^{-3}\ mm^{-1}}$ and $\Lambda_r = 8.2R^{-0.21}\ \mathrm{mm^{-1}}$.

VII. APPENDIX B. PARTICLE SIZE DISTRIBUTION: EQUIVALENT SPHERES

In this chapter, a particle is defined as being *equivalent* to a sphere if it has the same volume as a given sphere. However, other definitions of *equivalent* spheres appear in the literature, for example, definitions based on a sphere and spheroid having equal average projected areas. Let the quantity $N_c(r_c)$ be defined as the particle size distribution for an ensemble of spheroids, where r_c is the radius of a sphere that has a cross-sectional area equal to the average projected area of randomly oriented spheroids, and let $N(r_v)$ describe the same size distribution,

but in terms of r_v, the radius of a sphere that has a volume equal to that of a given spheroid. The purpose of this appendix is to relate $N_c(r_c)$ to $N(r_v)$. First, the radius of a sphere that has a volume equal to that of a given spheroid is written as

$$r_v = \left(a^2 b\right)^{1/3}, \tag{B1}$$

where a and b are the lengths of the particle nonrotational and rotational (symmetry) semi-axes. For prolate spheroids, the radius of a sphere that has a cross-sectional area equal to the average projected area of randomly oriented spheroids is given by (Mishchenko and Travis, 1994c)

$$r_c = \frac{1}{2}\left[2a^2 + \frac{2ab}{e}\arcsin e\right], \tag{B2}$$

and for oblate spheroids by

$$r_c = \frac{1}{2}\left[2a^2 + \frac{b^2}{e}\ln\frac{1+e}{1-e}\right], \tag{B3}$$

where the particle eccentricity is defined as

$$e = \frac{(\xi^2 - 1)^{1/2}}{\xi}, \tag{B4}$$

and the particle axial ratio ξ is defined as $\xi = b/a$ for prolate spheroids and $\xi = a/b$ for oblate spheroids. The ratio of the equal-surface-area sphere radius to the equal-volume sphere radius for prolate spheroids is thus given by

$$\frac{r_c}{r_v} = \left[\frac{1}{2}\left(\xi^{-2/3} + \frac{\xi^{1/3}}{e}\arcsin e\right)\right]^{1/2}, \tag{B5}$$

and for oblate spheroids by

$$\frac{r_c}{r_v} = \left[\frac{1}{4}\left(2\xi^{2/3} + \frac{\xi^{-4/3}}{e}\ln\frac{1+e}{1-e}\right)\right]^{1/2}. \tag{B6}$$

To compute an expression involving $N(r_v)$ when given $N_c(r_c)$, r_c may be computed using Eq. (B5) or (B6) and then substituted into the expression involving $N(r_v)$. For example, the ice water content (IWC) is computed using

$$\mathrm{IWC} = \rho_i \frac{4}{3}\int_{r_{v,\min}}^{r_{v,\max}} \pi r_v^3 N(r_v)\,dr_v, \tag{B7}$$

where ρ_i is the density of ice. Observing that

$$dr_v = \frac{r_v}{r_c}\,dr_c, \tag{B8}$$

the expression for ice water content may be rewritten in terms of $N_c(r_c)$ as

$$\mathrm{IWC} = \rho_i \frac{r_v}{r_c} \frac{4}{3} \int_{r_{c,min}}^{r_{c,max}} \pi r_c^3 N_c(r_c)\, dr_c. \quad \text{(B9)}$$

VIII. APPENDIX C. USE OF POWER LAW DISTRIBUTION IN T-MATRIX METHOD

Mishchenko and Travis (1994c) suggested that the scattering properties of an ensemble of randomly oriented spheroids are nearly independent of the shape of the size distribution, but instead depend primarily on the effective radius and effective variance (r_{eff} and v_{eff}) of the distribution. Because the T-matrix method admits an efficient solution for integration over a power law size distribution, the resulting scattering computations for the power law distributions of spheroidal particles can be obtained much more rapidly than for other size distributions. For this paper, numerical experiments were performed to confirm whether this result also applies for microwave frequencies. This was done by specifying a gamma drop size distribution of spheroidal particles and then numerically integrating the scattering properties over the distribution to obtain the scattering properties of the ensemble. Simultaneously, r_{eff} and v_{eff} were computed and used as parameters of a power law distribution (as described by Mishchenko and Travis, 1994c), and the ensemble scattering properties were computed and compared with those obtained using the gamma distribution. It was found that, because the power law size distributions used in this paper had finite size limits, all radiative cross sections obtained using the two methods agreed well so long as those obtained using the power law distribution were multiplied by the ratio of average geometric cross-sectional areas computed using finite power law distribution versus infinite gamma distribution limits.

ACKNOWLEDGMENTS

Thanks to Frank Evans for providing his polarized radiative transfer and "dda" codes, to Mike Mishchenko for providing his T-matrix codes, and to Piotr Flatau and Bruce Draine for providing their "ddscat" code. Thorough reviews of the initial draft of this chapter were given by Joop Hovenier, Frank Evans, and Ted Smith. Witek Krajewski, Chris Kummerow, and Ted Smith have served as my mentors over the last several years. I also acknowledge valuable discussions with Harry Czekala, Joe Turk, Quanhua Liu, and K.-H. Ding. Kevin Berney helped with some of the computations and figures while he was a student in the 1996 NASA/GSFC Summer Institute on Atmospheric and Hydrospheric Sciences. Thanks to Jim Cornelius and others at FNMOC and the United States Navy for their support.

Chapter 18

Polarized Light Scattering in the Marine Environment

Mary S. Quinby-Hunt
Lawrence Berkeley National Laboratory
University of California
Berkeley, California 94720

Patricia G. Hull
Department of Physics
Tennessee State University
Nashville, Tennessee 37209

Arlon J. Hunt
Lawrence Berkeley National Laboratory
University of California
Berkeley, California 94720

I. INTRODUCTION

This chapter discusses polarized light scattering in the marine environment with emphasis on scattering from nonspherical particles. The marine environment is extensive; the oceans cover approximately 70% of Earth's surface. The marine environment encompasses not only the world's oceans, but the atmosphere above it as well as floating sea ice. Light propagating through the marine environment

Light Scattering by Nonspherical Particles: Theory, Measurements, and Applications